

RESEARCH ARTICLE | DECEMBER 02 2022

Experimental study of the spray characteristics of twin-fluid atomization: Focusing on the annular flow regime

Chang Liu (刘畅); Kun Wu (吴坤) ; Zhenyu Zhang (章振宇); ... et. al



Physics of Fluids 34, 123309 (2022)

<https://doi.org/10.1063/5.0128231>



View
Online



Export
Citation

CrossMark

Articles You May Be Interested In

Experimental analysis of supercritical-assisted atomization

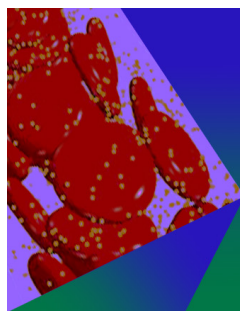
Physics of Fluids (January 2021)

A review on spray characteristics of effervescent atomizer under various geometrical parameters and operating condition

AIP Conference Proceedings (June 2012)

Combined drop sizing using phase Doppler anemometry and high-speed imaging

AIP Conference Proceedings (February 2023)



Physics of Fluids

Special Topic: Flow and Forensics

Submit Today!

Experimental study of the spray characteristics of twin-fluid atomization: Focusing on the annular flow regime

Cite as: Phys. Fluids **34**, 123309 (2022); doi: 10.1063/5.0128231

Submitted: 27 September 2022 · Accepted: 4 November 2022 ·

Published Online: 2 December 2022






View Online



Export Citation



CrossMark

Chang Liu (刘畅),^{1,2}  Kun Wu (吴坤),^{1,a)}  Zhenyu Zhang (章振宇),³  Yueming Yuan (袁越明),¹
and Xuejun Fan (范学军)^{1,2}

AFFILIATIONS

¹State Key Laboratory of High Temperature Gas Dynamics, Institute of Mechanics, Chinese Academy of Sciences, Beijing 100190, People's Republic of China

²School of Engineering Science, University of Chinese Academy of Sciences, Beijing 100049, People's Republic of China

³School of Mechanical Engineering, Beijing Institute of Technology, Beijing 100081, People's Republic of China

^{a)} Author to whom correspondence should be addressed: wukun@imech.ac.cn

ABSTRACT

The characteristics of twin-fluid atomization operating in the annular flow regime were studied experimentally under various gas-to-liquid ratios (GLRs) and injection pressures. The macroscopic morphology of the spray was obtained by shadowgraph, while the droplet size and velocity were measured using a phase-Doppler particle analyzer technique. It was found that the spray cone angle increases almost linearly with the GLR, and the axial distance required for droplet coalescence to outweigh the breakup decreases with increasing GLR. The Sauter mean diameter (SMD) first decreases and then increases along the axial direction due to the competition between turbulent breakup and droplet coalescence. The droplet size follows a lognormal distribution; the droplet velocity distribution is closer to a lognormal distribution under large GLRs, while it follows normal distribution with GLR = 3%. Regarding the radial distribution, low GLRs (3% and 5%) lead to a bimodal spatial velocity distribution, while for large GLRs, the droplet velocity decreases monotonically toward the far field. The spray tends to become more stable with increasing GLR and injection pressure P_{inj} , whereas the SMD increases with increasing P_{inj} . The underlying atomization mechanism in a twin-fluid injector in the annular flow state can be regarded as the disintegration of the initial liquid sheet by longitudinal Kelvin-Helmholtz instability followed by transverse Rayleigh-Taylor instability, which yields a direct proportionality of the droplet size to the initial liquid sheet thickness Δ_L . Subsequently, for high P_{inj} , the gas core shrinks and Δ_L increases, which results in an increased SMD but enhanced atomization efficiency Δ_L/SMD .

Published under an exclusive license by AIP Publishing. <https://doi.org/10.1063/5.0128231>

I. INTRODUCTION

In liquid-fueled scramjet engines, due to the extremely limited residence time for mixing and combustion, the atomization of the liquid fuel has a substantial impact on the subsequent ignition, flame holding, and overall combustion efficiency. For a scramjet combustor, the atomization effect mainly refers to two considerations.¹ First, the liquid fuel is scattered into small polydisperse droplets through the injector, which increases the specific surface area of the fuel and enhances the evaporation and mixing processes. The minimum ignition energy of the spray is proportional to the 4.5 power of the diameter of the droplet, indicating that smaller droplets require a notably lower ignition energy.² Second, the penetration height of the fuel spray needs to be considered, as a low penetration height may cause the fuel

to accumulate near the engine wall, resulting in low combustion efficiency.³ Consequently, for the optimal design of scramjets, developing appropriate injection techniques to control both the atomization quality and penetration height is of great significance.

Recently, operating in a wide space-speed range⁴ has been one of the main concerns of hypersonic propulsion, with the premise of ensuring that the engine works stably over a wide range of working conditions. To be more specific, for liquid fuel injection and atomization with a prescribed injector geometry, achieving a required atomization quality and penetration height is more feasible when using active control strategies,⁵ such as pulsed injection,⁶ swirling injection,⁷ or plasma-assisted atomization.⁸ Among these control strategies, twin-fluid atomization is considered to be a highly practical yet effective

approach, and this has been applied in fields including internal combustion engines,⁹ petrochemicals,¹⁰ and food-drying technology.¹¹

For scramjet engines, twin-fluid atomization technology has mostly been studied using experiments. Lin *et al.*¹² first applied twin-fluid atomization to a ramjet almost two decades ago, and they conducted experimental analysis of the spray structure in supersonic cross flow. It was found that with the addition of gas, the spray became denser, and the diameters of the spray droplets decreased. Subsequent study¹³ found that the penetration height of the spray increases with increasing gas volume fraction. Based on Lin *et al.*'s work, Yu *et al.*¹⁴ further studied the effect of twin-fluid atomization in a scramjet combustor. They suggested that twin-fluid atomization could reduce the spray droplet size, but the penetration height was mainly determined by the injection pressure. Recently, Chakraborty *et al.*¹⁵ experimentally investigated the characteristics of twin-fluid atomization combined with strut injection in a ramjet engine. It was observed that the Sauter mean diameter (SMD) of the spray decreased significantly with increasing gas-to-liquid ratio (GLR), but this effect began to gradually diminish as the GLR exceeded 20%.

Although the specific configurations of twin-fluid injectors may differ, their atomization process is mainly dictated by the flow regime of the gas–liquid two-phase flow inside the injector.¹⁶ In effervescent atomization, as proposed by Lefebvre *et al.*¹⁷ in the 1980s, the internal flow regime resembles that shown schematically in Fig. 1(a); the gas and liquid are uniformly mixed inside the injector to create a bubbly flow, and a pressure difference is formed between the mixing chamber and the injector orifice due to the convergence section. When this bubbly flow is ejected, the severe pressure difference causes the bubbles to rapidly expand and rupture, which leads to high-quality atomization. However, a subsequent study by Sun *et al.*¹⁸ showed that although the bubbly flow has the highest utilization rate of the gaseous medium, irregular bubble bursting unavoidably leads to spray instability, and the formation of elongated bubbles or continuous gas cores inside the injector is the key to achieving a stable spray.

Under relatively large GLRs, an annular liquid sheet will be formed inside the injector, as shown in Fig. 1(b). In this flow regime, as indicated by Matouš *et al.*,¹⁹ there are two effective physical processes involved in the atomization. On the one hand, the large slip velocity between the gas and liquid causes a severe shear effect on the

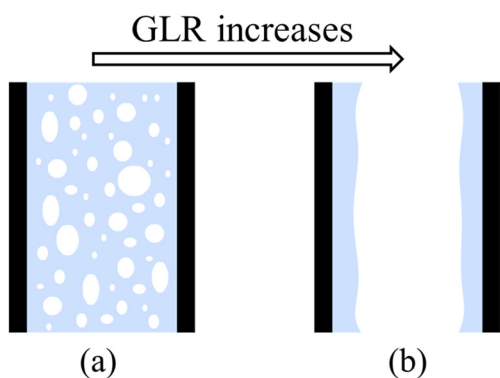


FIG. 1. Flow regime inside a twin-fluid injector operating in (a) bubbly flow and (b) annular flow. The blue and white colors denote the liquid and gas medium, respectively.

liquid sheet; on the other hand, the pressure difference between the gas core and the surrounding environment leads to considerable volume expansion. For the shear effect arising from the large slip velocity, the liquid film instability mechanism is similar to that of a gas–liquid coaxial jet. Catlin and Swithenbank²⁰ found that when the liquid film was issued from the injector orifice, the liquid film instability in the near field was dominated by the Kelvin–Helmholtz (K–H) instability. The viscosity and surface tension will prevent the liquid from breaking up, and the final atomized droplet diameter is mainly determined by the initial liquid film thickness. For the expansion effect of the internal gas core, Matouš *et al.*¹⁹ combined the experimental observations with modal decomposition and confirmed that the expansion effects of internal bubbles and gas cores play an important role in the two-fluid atomization.

For highly compressible twin-fluid atomization, Menon and Mohana²¹ studied the evolution of the spray in a two-phase supersonic overexpansion air jet; they found that compressible flow structures such as shock and expansion waves in the high-speed two-phase flow can induce collision and coalescence regimes through flow dynamics. Moreover, Wilson and Strasser²² examined two-fluid atomization for a non-Newtonian fluid and observed that the shock wave caused by the high-speed gas expansion promotes the wave formed by the viscosity gradient and Rayleigh–Taylor (R–T) instability, leading to sufficient atomization.

However, an experimental study by Wu *et al.*²³ postulated that the effect of bubbles or gas cores in twin-fluid atomization is twofold: the bubbles reduce the density of the gas–liquid mixture and shorten the wavelength of the hydrodynamic instability on the jet surface rendering finer droplets; nevertheless, the bubbles also increase the liquid's apparent velocity and decrease the relative velocity between the co-flowing air and gas–liquid mixture streams, which increases the droplet diameter. The resultant droplet diameter is, thus, determined by the competition between these two effects, which demonstrates the complexity of two-fluid atomization in annular flow regime.

Many different injector structures have been proposed to leverage the high-efficiency atomization of the above-mentioned twin-fluid configuration. Stähle *et al.*²⁴ proposed an injector design termed as “air-core-liquid-ring” atomizer to establish favorable annular flow within the outlet orifice; however, this was later found to be unstable at low GLRs by Kleinhans and coauthors.²⁵ Mllkvik *et al.*²⁶ proposed the outside-in-liquid (OIL) injector to alleviate the spray unsteadiness by keeping an annular flow state inside the injector. Unfortunately, Farid *et al.*²⁷ concluded that even in the annular flow state, the OIL injector still embeds certain oscillations into the spray, which will deteriorate under low GLRs.²⁸ In addition, in gas–liquid–gas multiple coaxial injection, it was found that the dominant frequencies of the unstable oscillation of the liquid film differ under different GLRs,²⁹ which reflects the trade-off between the shear and volume-expansion effects under different operating conditions. Regarding the factors influencing twin-fluid atomization in an annular flow state, Zhao *et al.*³⁰ pointed out that the atomized droplet size is positively related to the liquid film thickness and \sqrt{We} (where We is the Weber number), which was also confirmed by the experiments of Wachter *et al.*³¹ and Wintter *et al.*³²

As a result of the intricate interactions between the gas and liquid streams in an OIL twin-fluid injector, there are three aspects that need further investigation. First, more in-depth analyses of the disintegration

of the liquid ring and the subsequent atomization processes are needed. Second, the spray unsteadiness behavior under various operating conditions in terms of GLR and injection pressure is also not clear. Third, an increase in injection pressure will lead to a shrunken gaseous core, which, in turn, will alter the upstream injection conditions, i.e., the

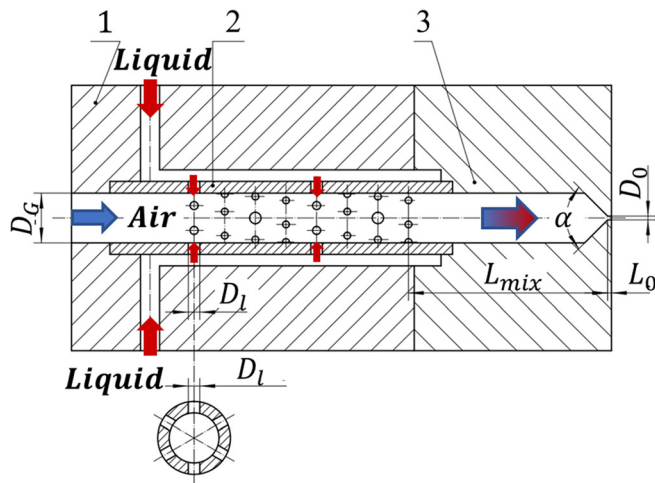


FIG. 2. Schematic diagram of the gas-liquid twin-fluid injector. Module 1 is the inlet manifold of the gas and liquid streams, module 2 the liquid injection chamber, and module 3 the injector orifice section.

TABLE I. Design parameters of the injector.

Parameter	D_0 (mm)	L_{mix} (mm)	D_l (mm)	N	D_G (mm)
Value	1	52	3	48	13

initial liquid sheet thickness. Thus, this coupling effect of the injection pressure on the atomization of the OIL injector merits further investigation.

Correspondingly, the present work examined the underlying mechanism of the atomization processes of a twin-fluid injector operating in an annular flow regime. The measurements examined the macroscopic structure of the spray and the associated flow state inside the injector using high-speed imaging, and droplet dynamic analyses were conducted based on phase-Doppler particle-analyzer (PDPA) measurements. In addition, we focused on the influence of the GLR and injection pressure on the atomization characteristics.

The remainder of this paper is structured as follows. In Sec. II, we briefly introduce the configuration of the injector and the experimental methodology. In Sec. III, we present the experimental results and discussion of the atomization characteristics, along with examinations of the influences of different factors on the spray and its instability. Conclusions will be given in Sec. IV.

II. EXPERIMENTAL SETUP AND METHODOLOGY

A. Generation of the twin-fluid spray

The twin-fluid injector is composed of three modules, as shown in Fig. 2: module 1 is the inlet manifold of the gas and liquid streams, module 2 is the liquid injection chamber, and module 3 is the injector orifice section. In the present study, the diameter of the injection orifice D_0 was 1 mm. According to Farid *et al.*,²⁷ the annular flow inside the injector requires the liquid-gas momentum ratio $\phi_{lh} < 0.01$. The injector parameters affecting ϕ_{lh} are the diameter of the injection hole D_l , the number of injection holes N , and the diameter of the mixing chamber D_G . Although the mixing chamber length L_{mix} has no direct influence on the droplet size, the liquid film thickness in the mixing chamber increases with decreasing L_{mix}/D_G . As suggested by a previous study,³³ $\alpha = 90^\circ$ and $L_0/D_0 = 1$ were adopted in the present injector design. The injection holes are divided into eight rows,

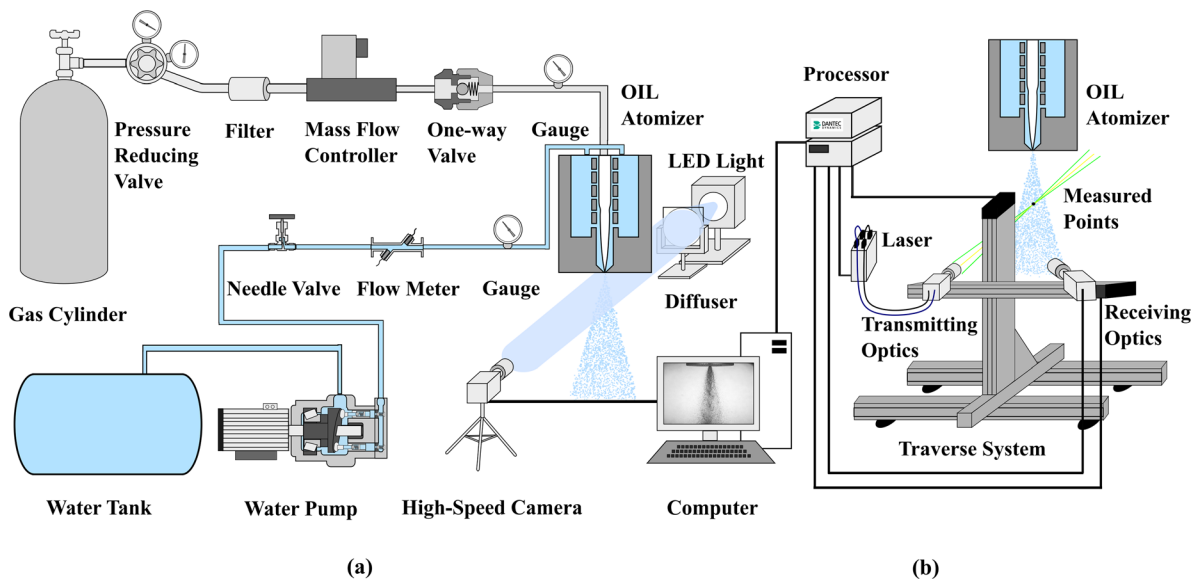


FIG. 3. Experimental facility and setup for (a) shadowgraph and (b) the PDPA system.

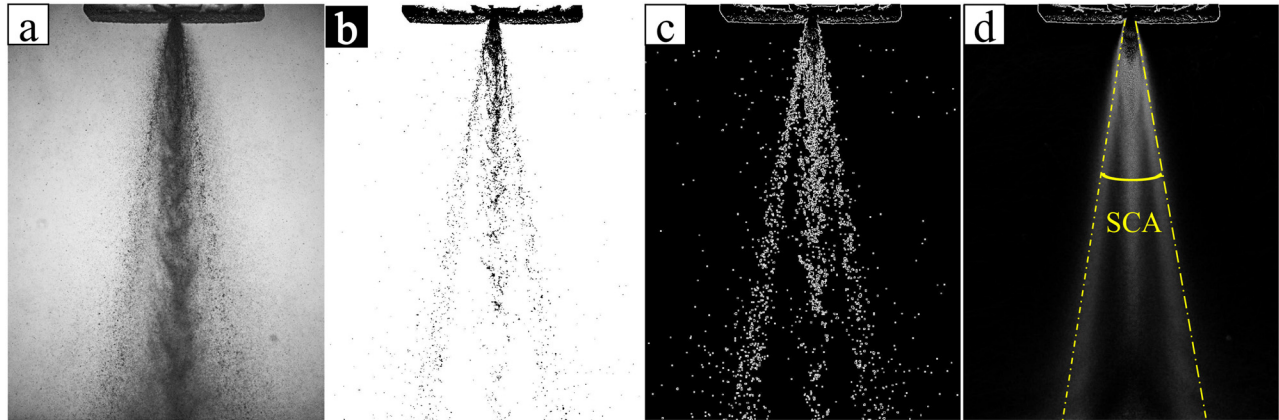


FIG. 4. Procedures for detecting the spray cone angle (SCA): (a) raw spray image, (b) binarization of the image, (c) extraction of the outline of the image, and (d) obtaining the average SCA.

with six injection holes evenly distributed for each row. To ensure uniformity in the circumferential direction, each neighboring injection row is rotated counterclockwise by 45°. The corresponding detailed design parameters are summarized in Table I. To facilitate

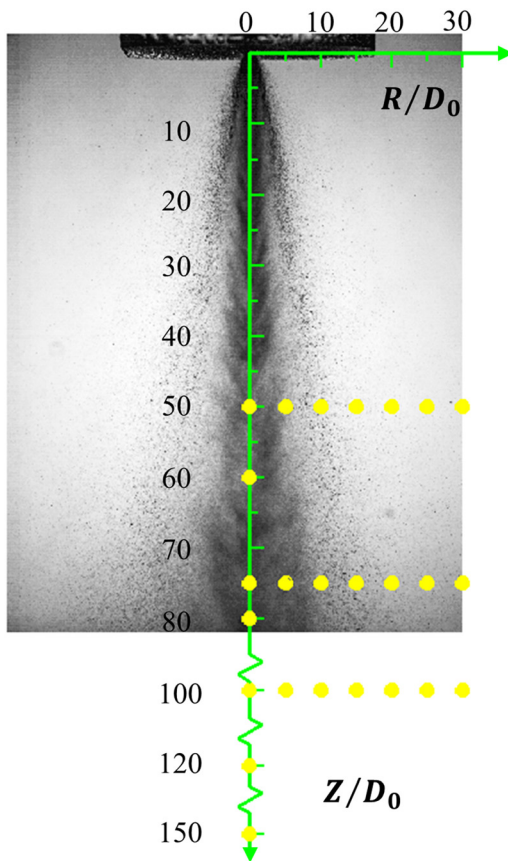


FIG. 5. Schematic diagram to show the PDPA sampling locations. The coordinate system is set up on the central axis of the spray.

visualization of the flow state inside the injector, it was made from high-quality acrylic.

The experimental setup is illustrated in Fig. 3(a), wherein all the following experiments were performed at temperature of 298 K and pressure of 101 325 Pa environment. GLR is defined as the ratio between the mass flow rates of the gas and liquid streams. In our experiment, the liquid stream was delivered by a plunger pump (Annovi Reverberi RC, 0–2 l/min), and the mass flow rate was controlled by the frequency converter (Eura Drives, E2000–0015T3). The corresponding mass flow rate m_l ranged from 5.2 to 22.14 g/s, and this was measured by an ultrasonic flow meter (KEYENCE, FD-XS8, 0–3000 ml/min, accuracy $\pm 0.3\%$ of the full scale). The liquid medium was water at 300 K with density $\rho_l = 1000 \text{ kg/m}^3$, dynamic viscosity $\mu_l = 10^{-3} \text{ Pa s}$, and surface tension $\sigma = 0.072 \text{ N/m}$. The gaseous stream employed high-purity compressed nitrogen delivered by a high-pressure gas cylinder. The upstream driven pressure was adjusted by a pressure-regulation valve, and the mass flow rate of the gaseous stream was regulated by a gas mass flow controller (ASERT, AST10-DB, 0–200 SLM, accuracy $\pm 1\%$ of the full scale). The injection pressures of both the liquid and gaseous streams were measured with pressure sensors (Westzh, CYB-20S, 0–3 MPa, accuracy $\pm 0.1\%$ of the full scale). To prevent backflow of the liquid, a one-way valve was installed in the gas pipeline. In each experimental test, both the mass flow rates of liquid stream and gaseous stream were prescribed, which corresponds to a determined GLR value.

It should be noted that due to the internal mixing nature of the twin-fluid injector, the pressures measured for the two streams are very similar. Therefore, they will both be denoted by a common pressure value ΔP_{mix} (with respect to the ambient pressure) in the following sections. For a typical operating condition of $m_l = 10.1 \text{ g/s}$ and GLR 10%,

TABLE II. Experimental uncertainties of SMD measurement by PDPA.

Z/D_0	GLR = 5%	GLR = 10%	GLR = 15%
50	0.020	0.017	0.032
100	0.014	0.003	0.004

the value of ΔP_{mix} corresponds to 0.80 MPa. During the experiments, the GLR was varied over a relatively large range (3%–20%) to investigate its influence. To compare the atomization effects under different injection pressures, experiments under three different ΔP_{mix} values, namely, 0.55, 0.80, and 1.2 MPa, were conducted. A comprehensive summary of the experimental parameters is provided in Tables S1 and S2 in the [supplementary material](#).

B. Visualization and measurement techniques

The external flow field of the spray was visualized using shadow imaging, as shown in [Fig. 3\(a\)](#). A 300 W diffused LED light source was used to illuminate the spray, and the spray morphology was captured by a high-speed camera (Phantom V711) with a macro lens (Tokina, AT-X M100 PRO D Macro, 100 mm $f/2.8$). The camera was set to a frame rate of 10 000 frames per second (fps), with an exposure time of 1.8 μs . The image size was 608×800 pixels, corresponding to a physical image resolution of 20 $\mu\text{m}/\text{pixel}$.

To analyze the image data from the macroscopic flow field, we employed MATLAB to process the captured images. The raw images

were first binarized. Due to the absorption of light in different spray area, in order to reconstruct the spray profile in the spray central plane, the image was converted into a binary image using adaptive threshold in MATLAB. The ForegroundPolarity parameter is set to dark to indicate that the foreground is darker than the background, and the sensitivity of the adaptive threshold is 0.5, thereby the contours of the image could then be extracted. Subsequently, the time-averaged spray cone angle (SCA) could be obtained from 1000 instantaneous spray snapshots. The corresponding image-processing steps are illustrated in [Fig. 4](#).

The droplet diameter and velocity were measured using a two-dimensional phase-Doppler particle anemometer (Dantec, FlowExplorer DPSS) as shown in [Fig. 3\(b\)](#). During the measurements, a multi-line argon-ion laser (0.12 W) generated horizontally polarized light and split it into two green ($\lambda = 532$ nm) and two yellow ($\lambda = 561$ nm) laser beams. The droplet diameter was measured using the second-order refraction mode of the phase-Doppler anemometer. The lens focal lengths of the transmitting and receiving probes were 750 and 1000 mm, respectively, and the angle between the two probes was 147° .

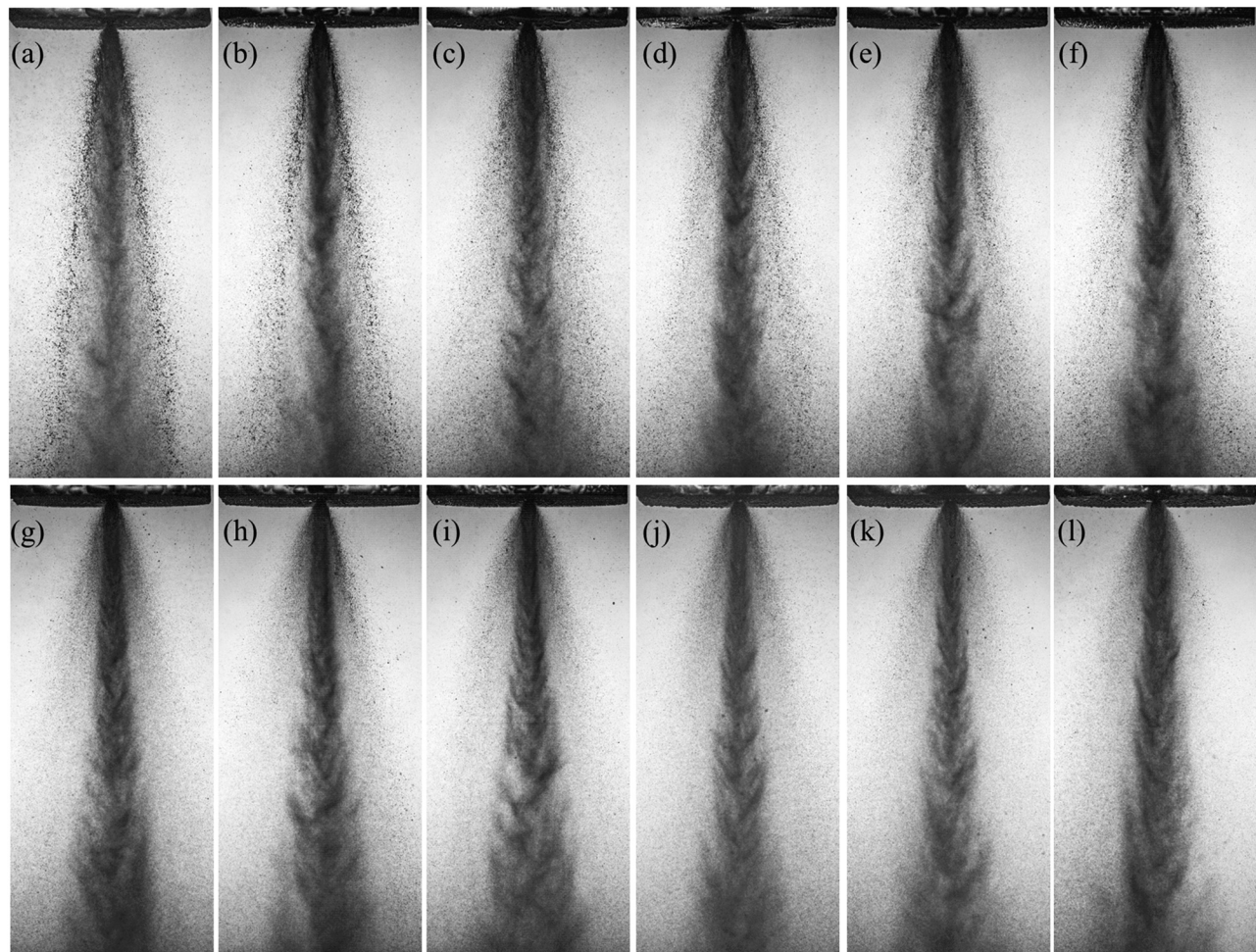


FIG. 6. Macroscopic morphology of the spray under $\Delta P_{\text{mix}} = 0.8$ MPa and various GLRs: (a) 3%, (b) 5%, (c) 6%, (d) 7%, (e) 8%, (f) 10%, (g) 12%, (h) 13%, (i) 14%, (j) 15%, (k) 18%, and (l) 20%.

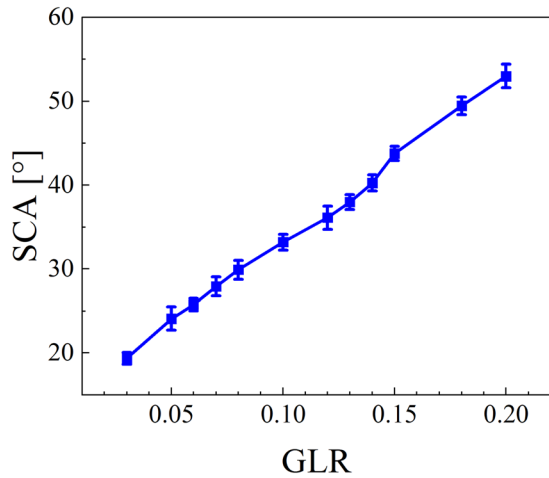


FIG. 7. SCA as a function of GLR under $\Delta P_{\text{mix}} = 0.8 \text{ MPa}$.

The droplet velocity was measured using the laser Doppler anemometer module, and the droplet size was obtained from the scattered yellow laser light.

Since the region very close to the injector has a high droplet number density and poor light transmission, the PDPA measurement locations need to be an appropriate distance away from the injector orifice. As generally accepted in previous studies,³⁴ a twin-fluid injector achieves primary atomization very close to the nozzle orifice, and, thus, most upstream measurements in the present work were conducted at $Z/D_0 = 50$ to ensure the sphericity requirement for PDPA detection. All the measurement locations are denoted by solid-circle symbols in Fig. 5. Measurement locations in the horizontal direction were equally arranged along $Z/D_0 = 50, 75,$ and 100 with an adjacent space of $R/D_0 = 5$ to obtain the radial distribution of the spray. The sampling time interval of each measurement location was set 10 s, with a maximum number of spherically valid samples of 100 000.

In this study, the PDPA measurements were repeated several times under each condition to quantify the measurement reliability.

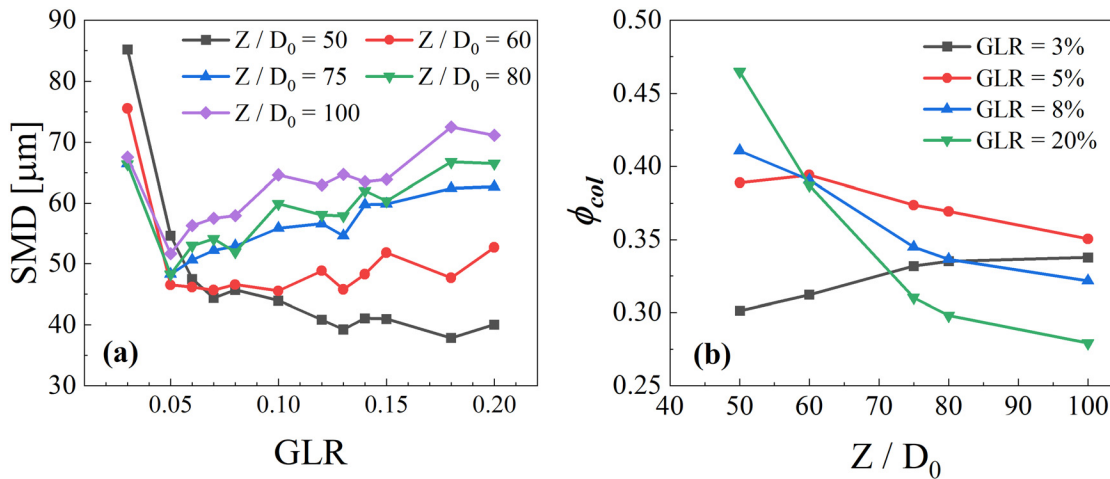


FIG. 8. (a) Droplet SMD variations as a function of GLR at five typical locations along the injector centerline under $\Delta P_{\text{mix}} = 0.8 \text{ MPa}$. (b) Probability of coalescence of the droplets at five typical locations along the injector centerline under $\Delta P_{\text{mix}} = 0.8 \text{ MPa}$ and various GLRs.

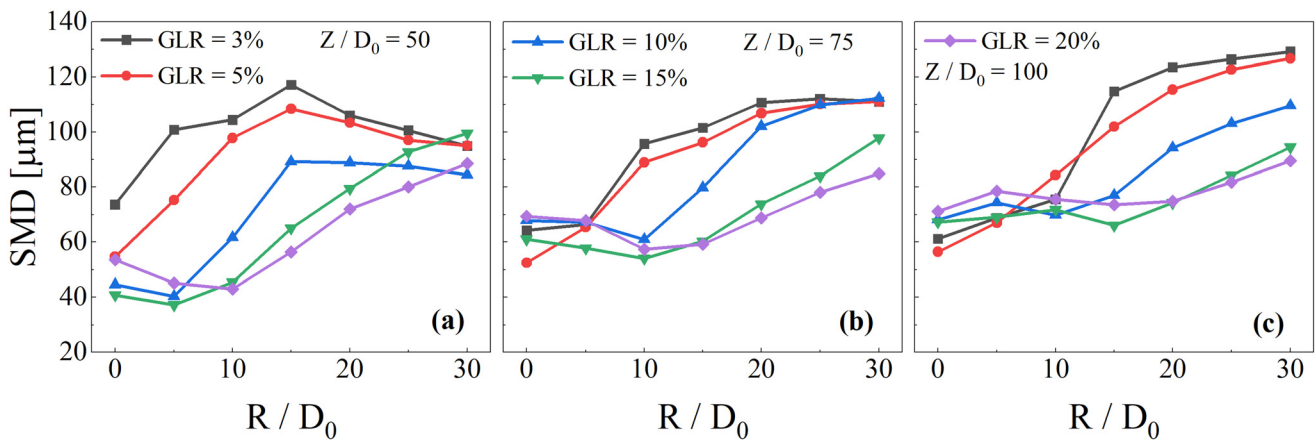


FIG. 9. Droplet SMD distributions with various GLRs under $\Delta P_{\text{mix}} = 0.8 \text{ MPa}$ along the horizontal direction at axial positions: (a) $Z/D_0 = 50,$ (b) $Z/D_0 = 75,$ and (c) $Z/D_0 = 100.$

Uncertainty analysis of the SMD (D_{32}) of the droplets was performed using the measurement data of three typical working conditions at two typical sampling locations $Z/D_0 = 50$ and 75 . The SMD is defined as

$$SMD = \frac{\sum N_i D_i^3}{\sum N_i D_i^2}. \quad (1)$$

The dimensionless uncertainty can be obtained as

$$U = \frac{S_i(\bar{x})}{\bar{x}} = \frac{\sqrt{\frac{\sum_k (x_k - \bar{x})^2}{n \times (n-1)}}}{\bar{x}}, \quad (2)$$

where x_k is the measured value for each dataset, n represents the total number of measurements, and \bar{x} represents the average value of the measurements. From the results in Table II, it can be seen that the uncertainty in the SMD measurements was below 5%.

III. RESULTS AND DISCUSSION

A. Macroscopic characteristics of the spray

The macroscopic morphologies of the spray under $\Delta P_{\text{mix}} = 0.8$ MPa with varying GLRs are shown in Fig. 6. As the annular liquid film emanated from the injector, the gas core, which is at sonic speed, moves much faster than the liquid film, while the slip velocity between the liquid film and the ambient is relatively small. This leads to severe atomization in the inner interface and moderate atomization in the outer region, yielding a bimodal distribution spray characteristic. As can be seen from Fig. 6(a), for the lowest GLR of 3%, the SCA is small, and there are large ligaments and liquid bulks at the outermost periphery of the spray. With increasing GLR, the atomization quality is obviously improved, and the spray plume near the gas core is more noticeable. It is also clear that, with increasing GLR, the SCA increases, and the boundary between the central gas core area and the peripheral low-speed crushing atomization area becomes more distinguishable.

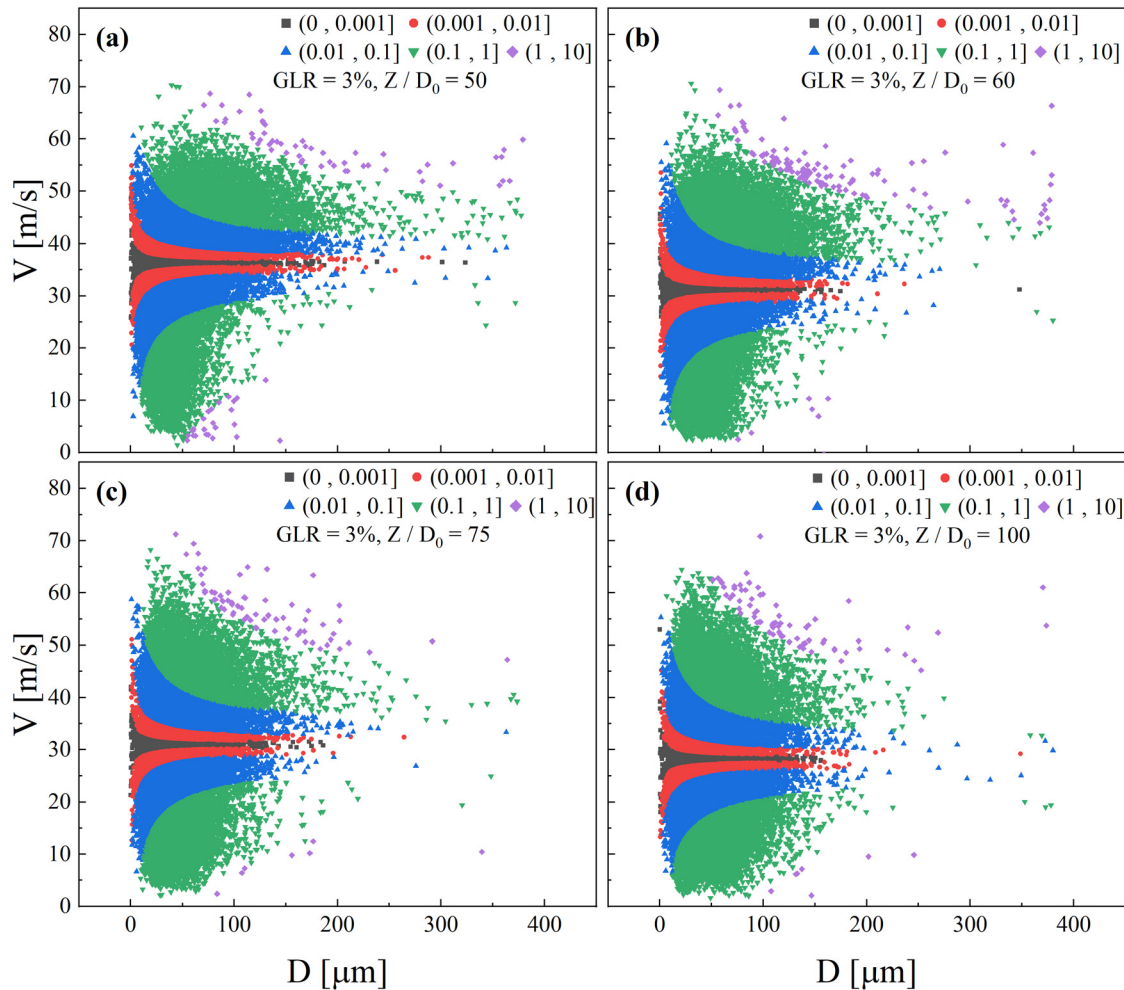


FIG. 10. Scatter plots of droplet diameters and velocities for GLR = 3% under $\Delta P_{\text{mix}} = 0.8$ MPa and four typical locations along the spray centerline, Z/D_0 : (a) 50, (b) 60, (c) 75, and (d) 100. The colors indicate corresponding binned We_S numbers.

The SCA was measured using the method described in Sec. II B, and the results are plotted in Fig. 7. The SCA increases almost linearly with GLR, which indicates that the spatial distribution of the spray becomes more uniform with increasing GLR.

The SMDs at five typical locations were obtained using the data sampled by PDPA. As shown in Fig. 8(a), for GLR = 3%, the droplets become successively smaller as the spray evolves downstream, which suggests that the gas–liquid interaction and droplet breakup still dominate at the position $Z/D_0 = 50$. Since the pressure in the mixing chamber remains constant for different GLR conditions, the mass flow rate of the liquid decreases with increasing GLR, while there is an inverse change in the mass flow rate of the gas flow stream. The shearing and gaseous expansion effects are strengthened, which leads to a shorter axial distance for the droplets to accomplish the breakup process. This tendency is further confirmed by the reduction in SMD at $Z/D_0 = 50$ with increasing GLR.

However, it is also noticeable that for $GLR \geq 5\%$, the SMD increases at the downstream locations regardless of the GLR.

This observation was also reported by Catlin *et al.*²⁰ and Wu *et al.*,³⁵ and it was attributed to droplet coalescence at downstream locations as the interaction between the two-phase flow attenuates. By following Wu *et al.*,³⁵ for a conservative estimation, we only consider head-on collisions between droplets. Therefore, the collision outcome is solely determined by the collision Weber number³⁶ ($We_{col} = \rho_l D_s U_{rel}^2 / \sigma$, where ρ_l is the liquid density, D_s is the diameter of the small droplet, and U_{rel} is the relative velocity between the colliding droplets).

Droplet coalescence is considered to occur when We_{col} is less than the critical value $We_{crit} = 20$; otherwise, separation will occur. Using 100 000 PDPA samples at each measurement location, the coalescence probability ϕ_{col} can be obtained.³⁷ As displayed in Fig. 8(b), for GLR = 3%, the probability of droplet coalescence increases as the droplets move downstream, which may result from the limited SCA rendering a concentrated spray cloud near the spray’s central region. In contrast, when the GLR exceeds 5%, the droplets are more likely to coalesce at upstream locations, suggesting that the coalescence effect of

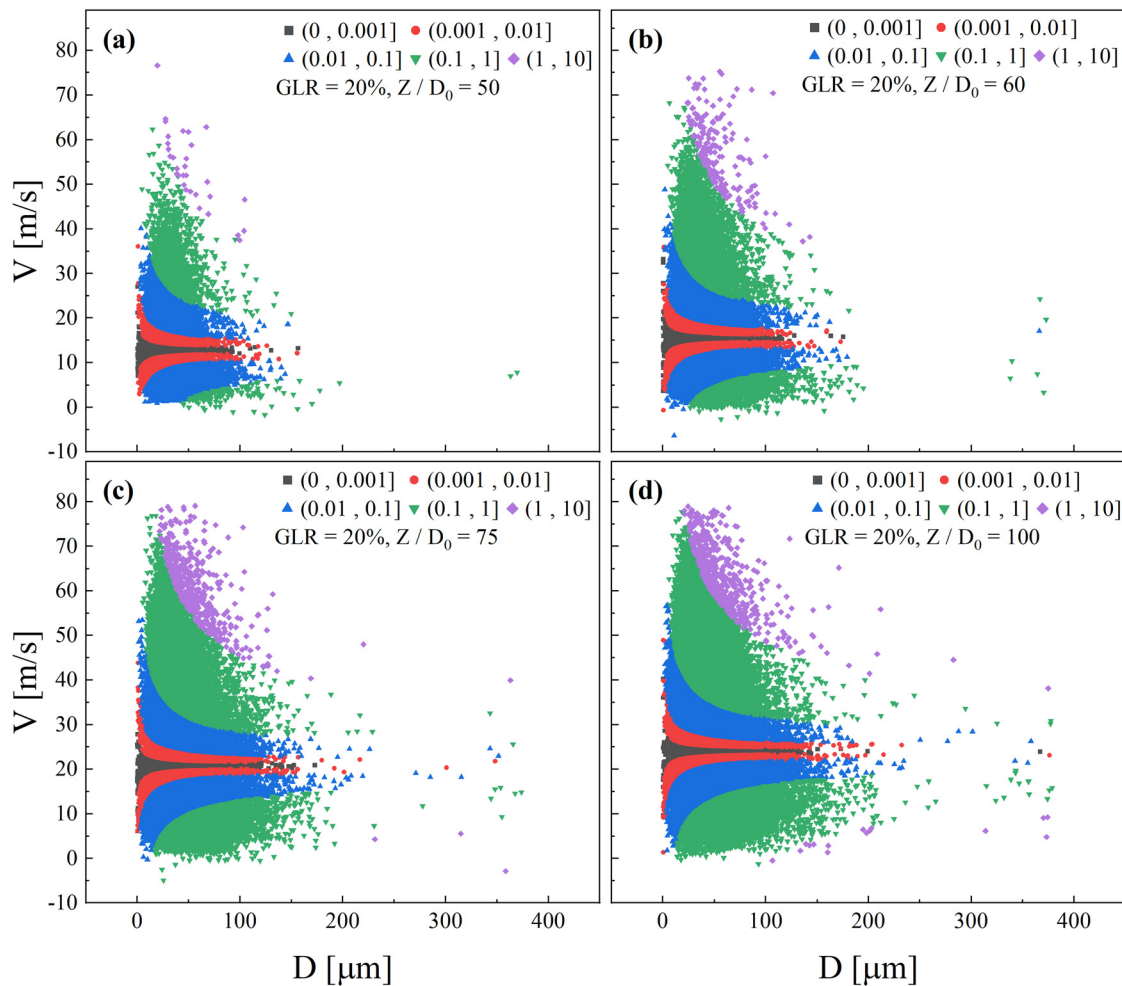


FIG. 11. Scatter plots of droplet diameters and velocities for GLR = 20% under $\Delta P_{mix} = 0.8$ MPa and four typical locations along the spray centerline, Z/D_0 : (a) 50, (b) 60, (c) 75, and (d) 100. The colors indicate corresponding binned We_s numbers.

droplets at this location is not negligible; this is also the reason for the increase in the SMD at downstream locations.

A comparison of the SMDs along horizontal lines at different streamwise locations with various GLRs is shown in Fig. 9. It can be observed that the SMD decreases with increasing GLR, and this general tendency is consistent with the results obtained along the spray centerline. In Fig. 9(a), the SMD for $GLR \leq 10\%$ embodies an inverted-V-type non-monotonically increasing trend, which is dictated by the bimodal atomization mechanism illustrated in Fig. 6. As the spray develops downstream, the inverted-V-type SMD distribution fades away as the spray continues to expand in the radial direction. In the meantime, the SMD also increases because the interaction between the gas core and the spray cloud becomes less pronounced at outer radial locations, which can be clearly observed in Figs. 9(b) and 9(c).

However, for $GLR \geq 10\%$, as presented in Fig. 9(a), the SMD shows a V-type non-monotonically increasing trend. This can be explained by the fact that at relatively large GLR, the entrainment of the central gas core flow becomes stronger and leads to a higher probability of droplet coalescence at the centerline region, which results in a local maximum value of SMD there. We also note that similar

deviation of the minimum value of SMD from the spray center region was also discussed by Sallam *et al.*³⁸ in a hollow swirling spray.

B. Statistical analysis on the droplet dynamics

Figure 10 presents scatter plots of the velocity and droplet size information at each measurement location under $GLR = 3\%$. In Fig. 10(a), the scattering of the droplet diameters is large, which indicates that the liquid bulks are not sufficiently disintegrated at $Z/D_0 = 50$. At downstream locations, the majority of the droplets are within the size range $0-200 \mu\text{m}$, and the occurrence of large droplets becomes relatively rare. Regarding the droplet velocity, it can be found that for small GLRs, a large number of droplets have velocities larger than 35 m/s at upstream locations ($Z/D_0 = 50$ and 60). As the spray evolves downstream in Figs. 10(c) and 10(d), droplets with large size and high velocity disintegrate into small ones, and these slow down due to the action of aerodynamic drag.

However, the distribution of droplet size and velocity shows a different pattern under $GLR = 20\%$, as presented in Fig. 11. By comparing Figs. 10 and 11, we can see that a larger GLR yields a smaller

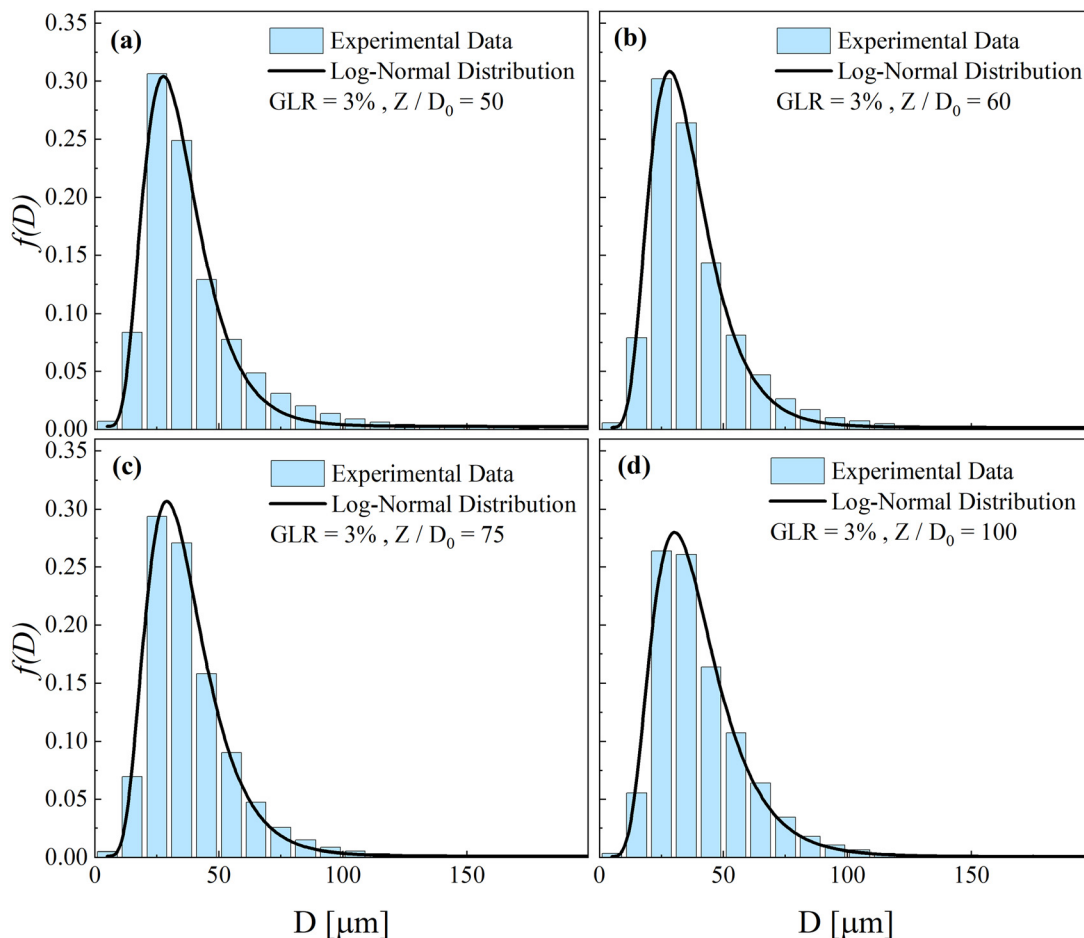


FIG. 12. Measured probability density functions (PDFs) of droplet diameter for $GLR = 3\%$ under $\Delta P_{\text{mix}} = 0.8 \text{ MPa}$ and four typical locations along the spray centerline, Z/D_0 : (a) 50, (b) 60, (c) 75, and (d) 100. The solid lines show fitted lognormal distributions.

droplet size, and the scattering range of droplet size also becomes relatively small. This implies that under constant mixing-chamber pressure, increasing GLR promotes the fragmentation of the liquid rim and shortens the axial distance required for full atomization. It is worth noting that, at downstream locations in Figs. 11(c) and 11(d), there are some exceptions whereby several slow-moving large droplets emerge due to coalescence between droplets.

The main difference between Figs. 10 and 11 in their diameter-velocity distribution patterns should be attributed to their different atomization states at the same spatial location. For GLR = 3%, the interaction between the two phases is limited, which leads to a greater axial distance for the secondary breakup process. Therefore, droplet breakup still dominates the atomization characteristics at $Z/D_0 = 50$ and 60. Conversely, for GLR = 20%, droplet breakup is greater before reaching the sampling locations, which leads to a coalescence-dominated region in the downstream locations.

To further scrutinize the droplet breakup dynamics when subjected to the high-speed gas core flow, we decomposed the turbulent motion into an average value and a fluctuation component.

Correspondingly, the forces acting on the droplets can be classified, as determined by the relative velocity between the droplets and the gas, and the turbulent flow carrying the fluid. To distinguish the breakup processes caused by these two effects, we refer to them as shear breakup and turbulent breakup, respectively.³⁹ Shear breakup occurs when a droplet is suddenly exposed to a relatively constant-velocity airflow if the shear Weber number We_s exceeds a critical value $(We_s)_C$.^{40,41} The shear Weber numbers of droplets measured at different measurement locations are also shown in Figs. 10 and 11. We_s is defined as

$$We_s = \frac{\rho_g (V_i - V_g)^2 D_i}{\sigma} > (We_s)_C, \quad (3)$$

where ρ_g represents the density of the droplet, V_i and V_g are the velocities of the droplet and gas flow at the measurement location, respectively, D_i is the diameter of the droplet, and σ is the surface tension coefficient. Since PDPA cannot be used to directly measure the gas velocity, in twin-fluid atomization, droplets with Stokes number $St < 1$ are often used to track the motion of the gas flow in their

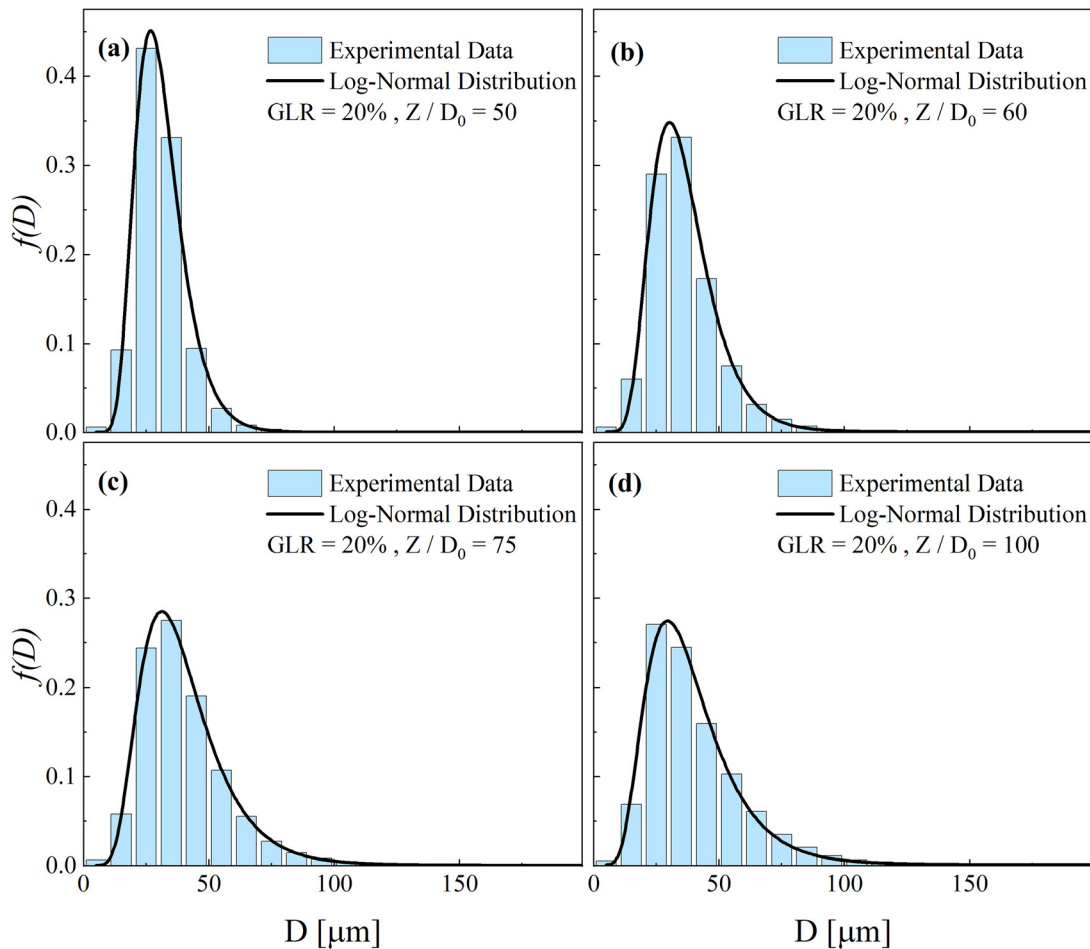


FIG. 13. Measured PDFs of droplet diameter for GLR = 20% under $\Delta P_{mix} = 0.8$ MPa and four typical locations along the spray centerline, Z/D_0 : (a) 50, (b) 60, (c) 75, and (d) 100. The solid lines show fitted lognormal distributions.

vicinity. According to Ferrand *et al.*,⁴² the gas flow velocity V_g is, therefore, represented by the average velocity of those droplets with diameters of 0–5 μm . A previous experimental study⁴³ suggests that the critical Weber number for viscous droplets is around 10. Here, we take $(We_s)_C = 10$ as a conservative estimation. The Weber numbers of the droplets are all within 10, which indicates that the secondary atomization in this study has the form of turbulent breakup.

TABLE III. Means and standard deviations of the fitting curves for the spray droplet diameter distributions.

Z/D_0	GLR = 3%			GLR = 20%		
	σ_D	μ_D	R^2	σ_D	μ_D	R^2
50	14.464	34.996	0.991	9.967	31.025	0.996
60	14.732	35.737	0.995	12.945	36.195	0.997
75	15.217	36.772	0.997	16.935	39.983	0.999
100	17.224	39.358	0.995	17.707	38.991	0.995

Accordingly, the gas Reynolds numbers in this study ranged from 10^4 to 10^5 , which also confirms turbulent breakup.

The distribution laws of the droplet size and velocity are of great significance for the in-depth understanding of the microscopic characteristics or the spray. Probability density functions (PDFs) of discrete droplet diameters and their lognormal fittings at various measurement locations along the spray centerline under different conditions are exhibited in Figs. 12 and 13. The lognormal distribution takes the following form

$$f(D; \mu_D, \sigma_D) = \frac{1}{\sqrt{2\pi}D\sigma_D} \exp\left[-\frac{(\ln D - \mu_D)^2}{2\sigma_D^2}\right], \quad (4)$$

where μ_D and σ_D denote the mean and standard deviation of the natural logarithm of the droplet diameter, respectively, as summarized in Table III. It can be observed that the fitting curves agree well with the experimental data. The droplet diameters are mostly distributed in the range 0–100 μm , and droplets with diameters of 0–75 and 0–50 μm account for the majority of the total samples for GLR = 3% and 20%, respectively. The values of μ_D and σ_D generally increase with

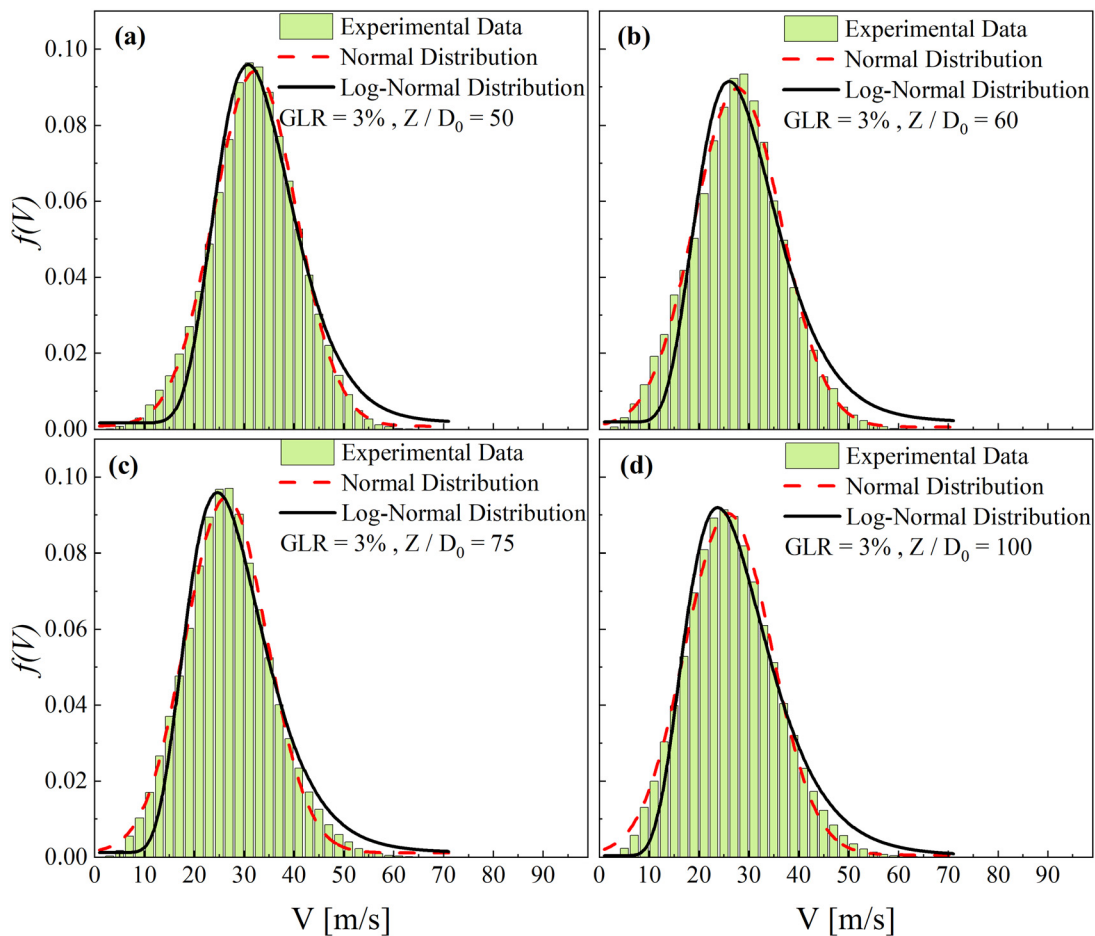


FIG. 14. Measured PDFs of droplet velocity for GLR = 3% under $\Delta P_{\text{mix}} = 0.8 \text{ MPa}$ and four typical locations along the spray centerline, Z/D_0 : (a) 50, (b) 60, (c) 75, and (d) 100. The solid black and dashed red lines show normal and lognormal distributions, respectively.

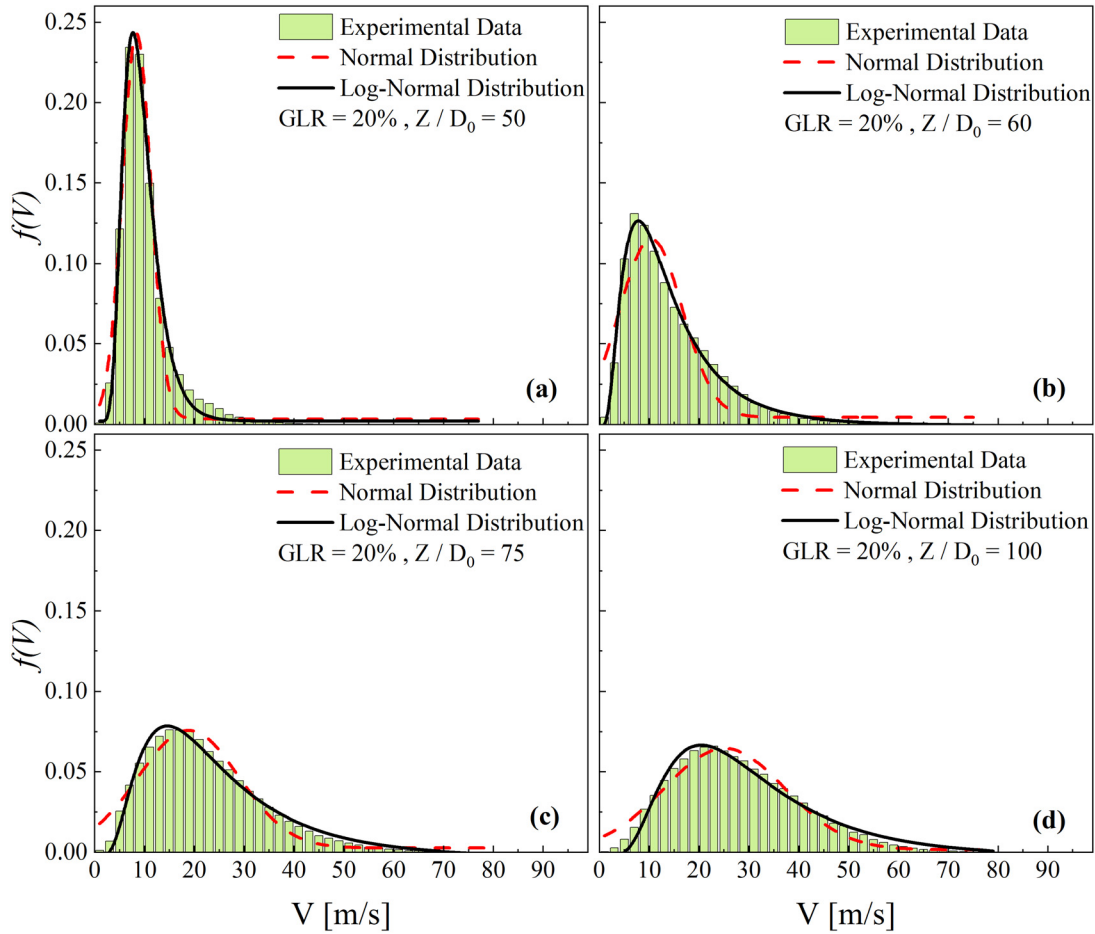


FIG. 15. Measured PDFs of droplet velocity for GLR = 20% under $\Delta P_{\text{mix}} = 0.8 \text{ MPa}$ and four typical locations along the spray centerline, Z/D_0 : (a) 50, (b) 60, (c) 75, and (d) 100. The solid black and dashed red lines show normal and lognormal distributions, respectively.

increasing streamwise distance for both GLR cases, with the peak value of $f(D)$ shifting to larger diameter values, indicating greater probability of droplet coalescence under GLR = 20% than GLR = 3%. This early coalescence again corroborates shorter primary and secondary breakup regimes with increasing GLR.

Figures 14 and 15 show PDFs of droplet velocity distribution at different measurement locations on the spray center axis under different operating conditions. The measurements of discrete droplet velocity are represented by the histogram of the number frequency $f(D)$, and these are fitted with both normal and lognormal distributions:

$$f(V; \mu_V, \sigma_V) = \frac{1}{\sqrt{2\pi}\sigma_V} \exp\left[-\frac{(V - \mu_V)^2}{2\sigma_V^2}\right], \quad (5)$$

$$f(V; \mu_V, \sigma_V) = \frac{1}{\sqrt{2\pi V}\sigma_V} \exp\left[-\frac{(\ln V - \mu_V)^2}{2\sigma_V^2}\right], \quad (6)$$

where μ_V and σ_V denote the means and standard deviations of the natural or log-natural logarithm of the droplet velocity, respectively, whose specific values are given in Table IV.

In line with Fig. 10, for GLR = 3%, the velocity distribution of the droplets is relatively uniform, so it tends to be a normal distribution, as indicated by the red dashed lines in Fig. 14. In addition, for the same GLR condition, the velocity distribution range becomes larger as the spray develops downstream, and the corresponding peak velocity also increases. Under large GLRs, as shown in Fig. 15, the overall PDF approaches lower velocities, the variation range of velocity distribution

TABLE IV. Means and standard deviations of the fitting curves for the spray droplet velocity distributions.

Z/D_0	GLR = 3%			GLR = 20%		
	σ_V	μ_V	R^2	σ_V	μ_V	R^2
50	8.592	33.819	0.977	3.592	9.413	0.994
60	9.330	29.919	0.953	11.201	15.0773	0.996
75	9.109	28.517	0.976	18.705	26.611	0.987
100	9.981	28.314	0.979	19.240	32.251	0.980

shrinks, and the peak value of the velocity distribution also becomes smaller at upstream locations, whereas the peak shifts to large velocity as the droplets are accelerated by the gas stream to the downstream locations. It can also be found that, for large GLRs, the velocity distribution is better characterized by the lognormal distribution, as quantified by the R^2 values in Table IV. Overall, these differences in both velocity and droplet diameter distribution functions for $GLR = 3\%$ and 20% also reflect the discordance in the atomization process in the axial direction under various GLRs. Similar results can also be observed for $GLR = 8\%$, as shown in Figs. S1–S3 and Tables S3 and S4 of the supplementary material.

C. Spray instability and associated internal flow

Twin-fluid atomization essentially involves a shear layer between two streams, wherein absolute instability and self-pulsation will invariably occur beyond a critical momentum flux ratio.^{44,45} Although Farid *et al.*²⁷ argued that a gas–liquid coaxial injector in the annular flow regime could produce a spray that is more stable than other injector configurations, it still exhibits spray fluctuations and variations in droplet dynamics under different GLR conditions.

For a qualitative comparison, the standard deviations of the spray were obtained by calculating the standard deviation of the gray value of 1000 shadow images during the quasi-steady state. A large standard deviation value in an area implies that the spray fluctuates more violently there over time. As shown in Figs. 16(a) and 16(b), under low GLRs (3% and 5%), the spray shows considerable fluctuations near the

interface between the high-speed gas core and the dense liquid region. As the GLR increases, the oscillation of the spray diminishes, implying better spray stability.

The instability of the spray is also embodied in the droplet dynamics. The velocities of droplets measured within 500 ms at the same measurement location under various GLRs are shown in Fig. 17. It can be clearly seen that when the GLR is relatively low (3% and 5%), the variation in the droplet velocity is remarkable. With continuous increase in GLR, the variation of the droplet velocity diminishes significantly, indicating that the spray becomes more stable, which is consistent with the previous statistical results. Similar results can also be found for the other two injection pressures, as shown in Figs. S4 and S5 of the supplementary material.

The characteristics of the external spray are dictated by the disintegration of the liquid sheet emanating from the injection orifice, which is further determined by the internal flow state between the two phases in the injector. Thus, the internal flow near the injector orifice was visualized using a microscope lens (Navitar, $12\times$ UltraZoom). The frame rate of the camera was 2000 fps, the exposure time was $60\ \mu\text{s}$, and the spatial resolution of the resulting images is $20\ \mu\text{m}/\text{pixel}$. It should be noted that, limited by the structural strength of the acrylic material, the injector wall is relatively thick ($30\ \text{mm}$), and the magnification of the lens was, thus, restricted to $7\times$ in the present work. In this regard, these visualization results should only be regarded as qualitative demonstrations of the internal flow state.

As displayed in Fig. 18, for low to intermediate GLRs, the liquid is flowing as a film along the inner wall in the mixing chamber, and it

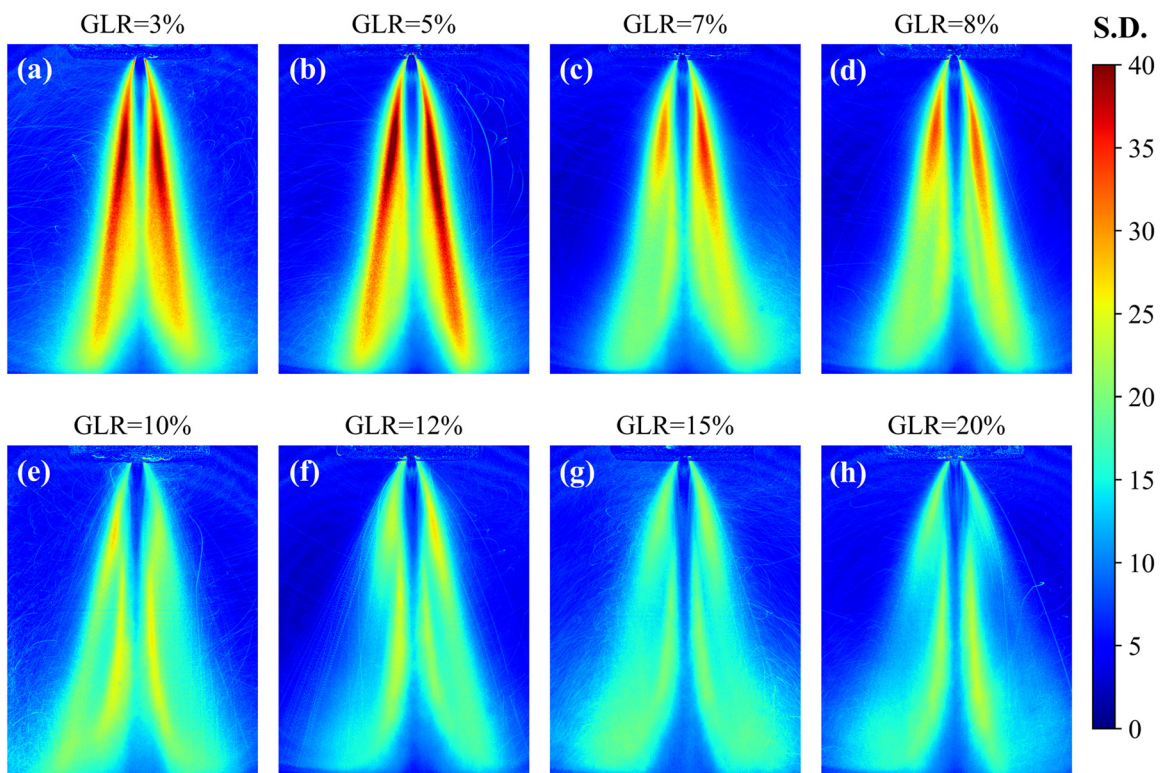


FIG. 16. Standard deviations under $\Delta P_{\text{mix}} = 0.8\ \text{MPa}$ and GLRs: (a) 3% , (b) 5% , (c) 7% , (d) 8% , (e) 10% , (f) 12% , (g) 15% , and (h) 20% .

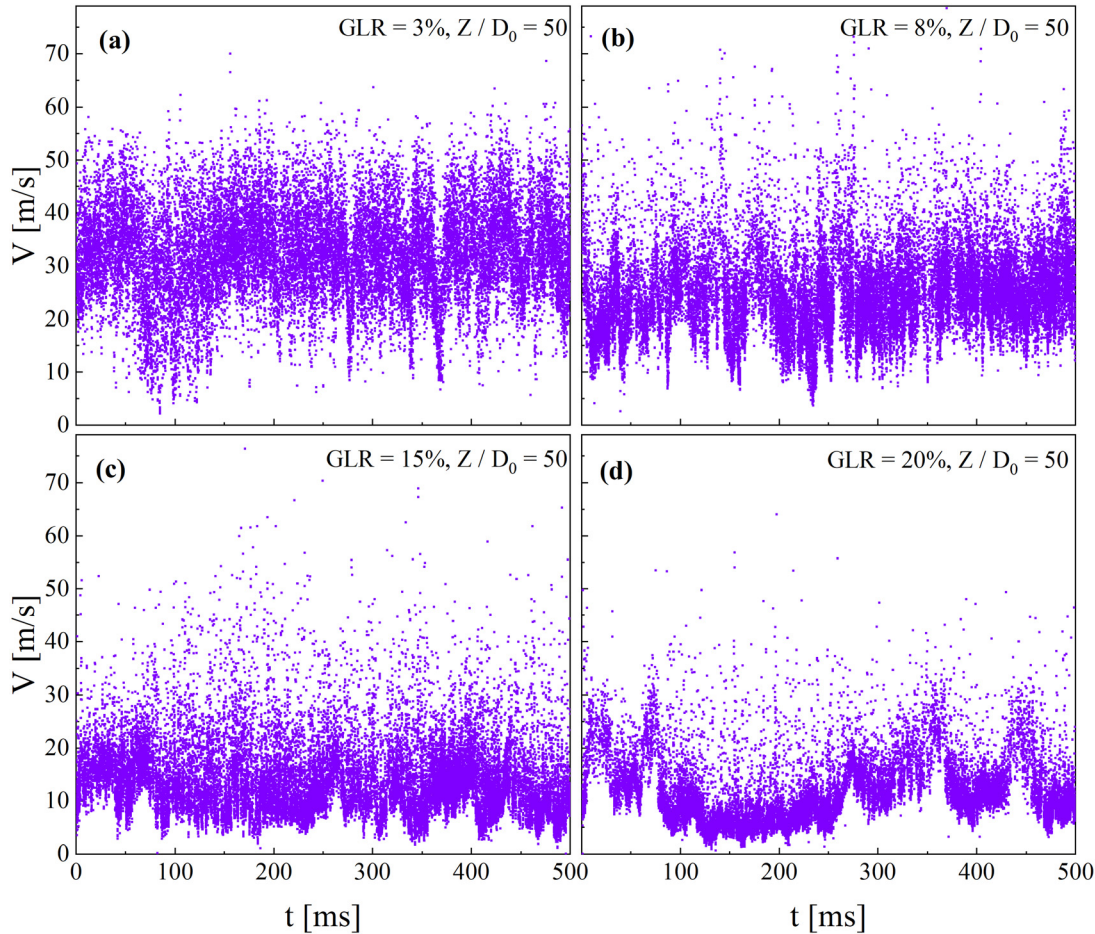


FIG. 17. Temporal evolution of droplet velocities and arrival times at $Z/D_0 = 50$ under $\Delta P_{\text{mix}} = 0.8$ MPa and four typical GLRs: (a) 3%, (b) 8%, (c) 15%, and (d) 20%.

becomes thinner as it passes through the convergence section and approaches the entrance to the injection orifice. By inspecting the image sequence, we can see that the precession of the central gas core is noticeable, and this leads to continual variation in the liquid sheet's thickness, rendering an unsteady spray under low to intermediate GLRs. In contrast, under large GLRs, the gas entering the convergence section nearly fills the full width, except for barely visible liquid films on the inner walls of the injector. Furthermore, the gas core remains relatively stable, which is consistent with the lower spray unsteadiness under high GLRs.

D. Influence of the injection pressure

Operating in the gas-core-liquid-ring flow state, the annular flow pattern is sustained by a continuous core of compressed gas in the middle of the liquid stream in the present injector configuration. Thus, gas plays two main roles in the atomization process: on the one hand, the gas squeezes the liquid sheet and strips it into ligaments and fragments when ejected from the injector; on the other hand, the gas abruptly expands to disintegrate the liquid fragments into droplets

when they issue through the orifice. Consequently, it is natural to speculate that an increase in injection pressure will also enhance the atomization quality by means of a greater expansion potential.³² Therefore, the effect of injection pressure will be further examined in this section.

The macroscopic morphologies of the spray under various ΔP_{mix} values and GLRs are shown in Fig. 19. It can be observed that, with increasing injection pressure, the SCA increases significantly, which is consistent with the quantitative results shown in Fig. 20. For low GLRs ($\leq 10\%$), the atomization improves, and in particular, the large ligaments around the outer periphery of the spray disappear as the injection pressure increases. As for large GLRs ($> 10\%$), the optical density of the spray periphery increases with increasing injection pressure, which means that finer droplets are produced under higher injection pressures.

The standard deviations of the spray at various ΔP_{mix} values and GLRs are shown in Fig. 21. It is evident that the standard deviation of the spray decreases significantly as the injection pressure increases. The spray tends to become stable with increasing GLR and also with increasing injection pressure. It can also be seen that under low injection pressures, imperfections in injector manufacturing lead to an

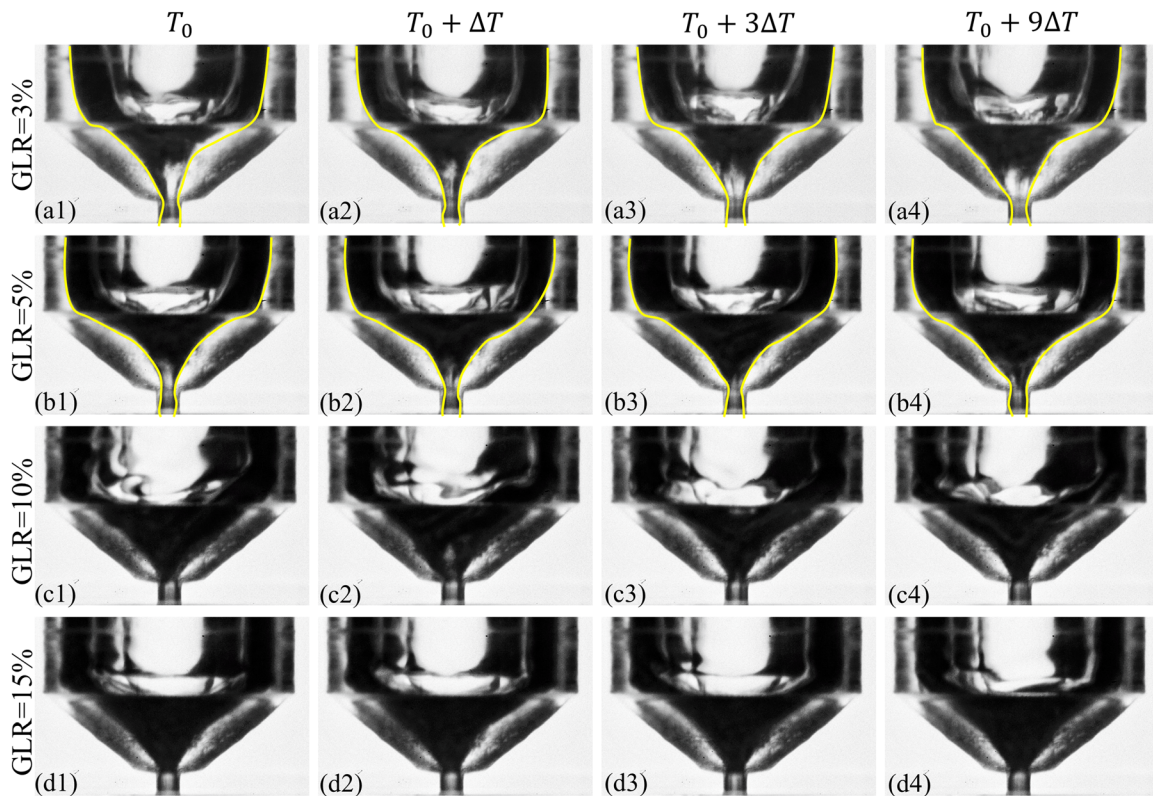


FIG. 18. Flow state in the mixing chamber with $\Delta T = 5$ ms under $\Delta P_{\text{mix}} = 0.8$ MPa and GLRs: (a1)–(a4) 3%, (b1)–(b4) 5%, (c1)–(c4) 10%, and (d1)–(d4) 15%. The interface between the gas and liquid phases is marked with yellow line.

obviously asymmetric spray morphology; this is alleviated under higher injection pressures.

To further quantify the stability of the spray, a dimensionless parameter $SD/Mean$ defined as the ratio between the spatial averaged standard deviation and the spatial averaged mean value of the gray values of the 1000 sample images. The corresponding results for three different operating pressures are displayed in Fig. 22. It can be seen that for low injection pressures $\Delta P_{\text{mix}} = 0.55$ and 0.80 MPa, the dimensionless standard deviation becomes lower than 10% as the GLR exceeds 10%. Nevertheless, for large injection pressure $\Delta P_{\text{mix}} = 1.20$ MPa, the spray is much more stable whose dimensionless standard deviation is always within 10% even at the smallest GLR condition.

A quantitative comparison of the SMDs at different positions along the spray center axis under different injection pressures and GLRs is shown in Fig. 23. For the lowest GLR (5%), the SMD first declines and then increases as the spray develops to the downstream locations, as exhibited in Fig. 23(a). Under intermediate GLRs (10% and 15%), the SMDs increase monotonically before reaching their maximum value with the development of the spray. However, for the largest GLR (20%), the SMD first increases at upstream locations, but it declines at downstream locations. This difference in SMD variation lies in the different axial evolution controlled by the competition between the droplet breakup and coalescence processes as well as the gas entrainment under various GLR and injection pressure conditions.

Furthermore, it is interesting that in Fig. 23(a), for the same GLR, the SMD under $\Delta P_{\text{mix}} = 1.20$ MPa is in between the values under $\Delta P_{\text{mix}} = 0.55$ and 0.80 MPa, whereas for $GLR \geq 10\%$, the SMD increases with increasing injection pressure. This tendency is somewhat inconsistent with the conviction that a higher injection pressure should result in a smaller SMD as more energy is consumed.^{46,47} Nevertheless, these previous understandings regarding the injection pressure are mainly limited to external mixing twin-fluid injectors⁴⁸ or bubbly flow effervescent injectors;¹⁴ the effect of injection pressure on the atomization efficiency is still not clear.

To reveal the physical mechanism leading to the anomaly in SMD variation as injection pressure increases, we need to fully understand the physical processes governing the atomization in the twin-fluid injector operating in annular flow state. Following Marmottant and Villermaux's investigation⁴⁹ of the liquid-core-air-ring configuration, a liquid sheet destabilization mechanism in the case of an annular flow state is tentatively proposed, and this is illustrated in Fig. 24.

The liquid destabilization is initialized by a longitudinal K–H instability, which generates interfacial waves on the liquid sheet by aerodynamic forces. In the second stage, the surface perturbations grow due to transverse R–T instability, wherein liquid ligaments protruding from the liquid ring are accelerated by aerodynamic interactions, leading to the disintegration of the intact liquid sheet.^{50,51} This process is referred to as the primary atomization; a secondary

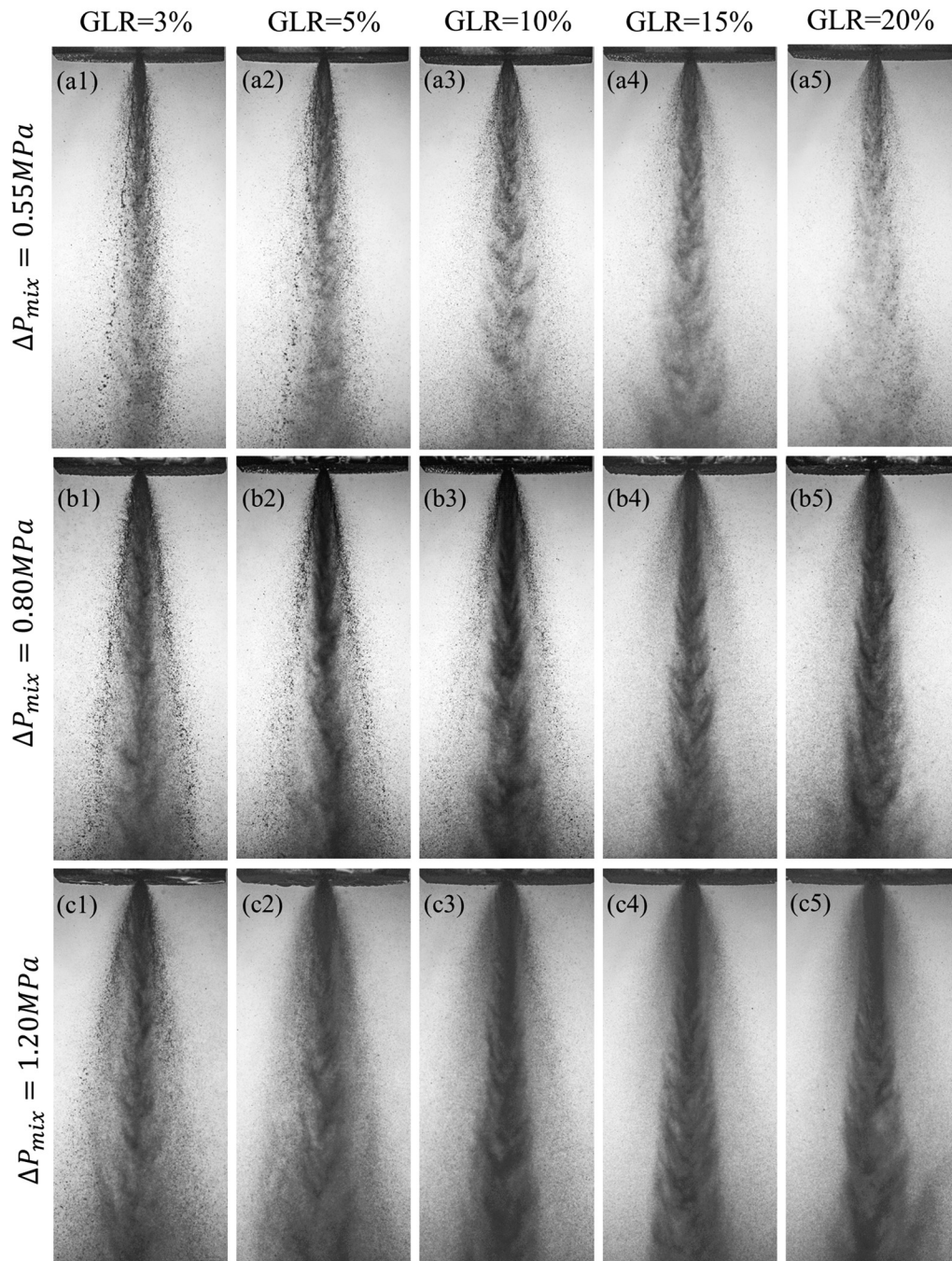


FIG. 19. Macroscopic morphology of the spray under various GLRs and ΔP_{mix} values in which (a1)–(a5) $\Delta P_{mix} = 0.55$ MPa, (b1)–(b5) $\Delta P_{mix} = 0.80$ MPa, and (c1)–(c5) $\Delta P_{mix} = 1.20$ MPa.

atomization will occur if the primary droplets exceed a critical size. The primary breakup process covers the formation of unstable waves along with the detachment of liquid ligaments, which controls the size, dynamics, and spatiotemporal distribution of the resultant spray. Therefore, the SMD is determined by the initial liquid sheet

thickness by successive longitudinal K–H instability and transverse R–T instability.^{52,53} Correspondingly, a rough estimation can be formulated as $SMD \propto \Delta_L^c$, where Δ_L is the initial liquid sheet thickness and c is a model constant, which was experimentally fitted to be 0.38 by Rizk and Lefebvre.⁵⁴

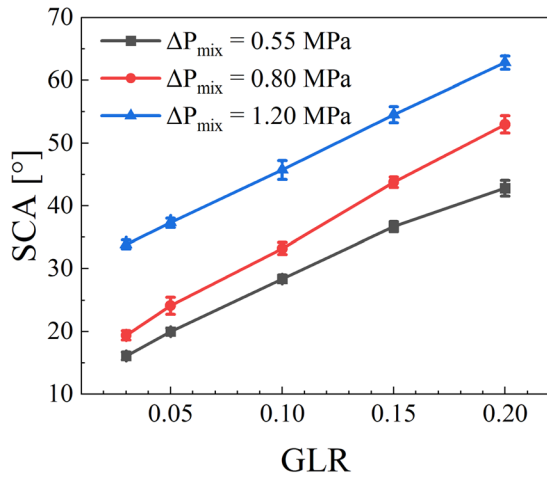


FIG. 20. SCA as a function of GLR under various ΔP_{mix} values.

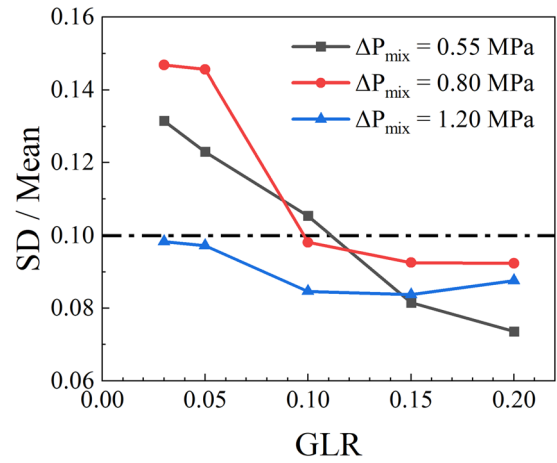


FIG. 22. Dimensionless standard deviations under various GLRs and ΔP_{mix} values.

According to the internal flow state shown in Fig. 18, the gas-liquid two phase flow forms an annular flow inside the injector with a distinguishable interface between gas and liquid streams. Since the absolute injection pressure $P_{inj} = \Delta P_{mix} + P_{amb}$ in the injector chamber is large enough to be choked at the injector orifice,⁵⁵ the gas flow

in the passage formed by the surrounding liquid film resembles that flow through a convergent injector as shown in Fig. 24. Therefore, the flow speed of the gas phase at the injector orifice is equivalent to the local sound speed.^{20,56} According to the relationship⁵⁵ between the critical parameters, area of the critical section A^* can be found,

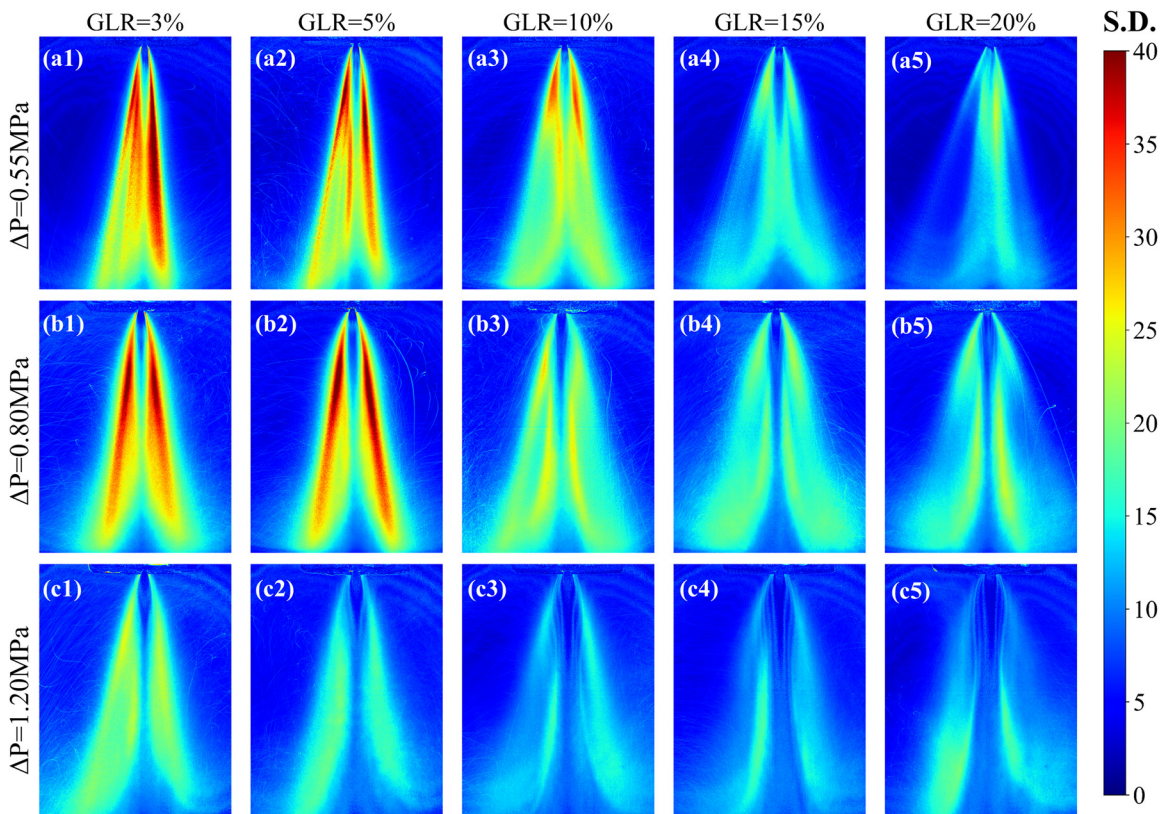


FIG. 21. Standard deviations under various GLRs and ΔP_{mix} values in which (a1)–(a5) $\Delta P_{mix} = 0.55$, (b1)–(b5) $\Delta P_{mix} = 0.80$, and (c1)–(c5) $\Delta P_{mix} = 1.20$ MPa.

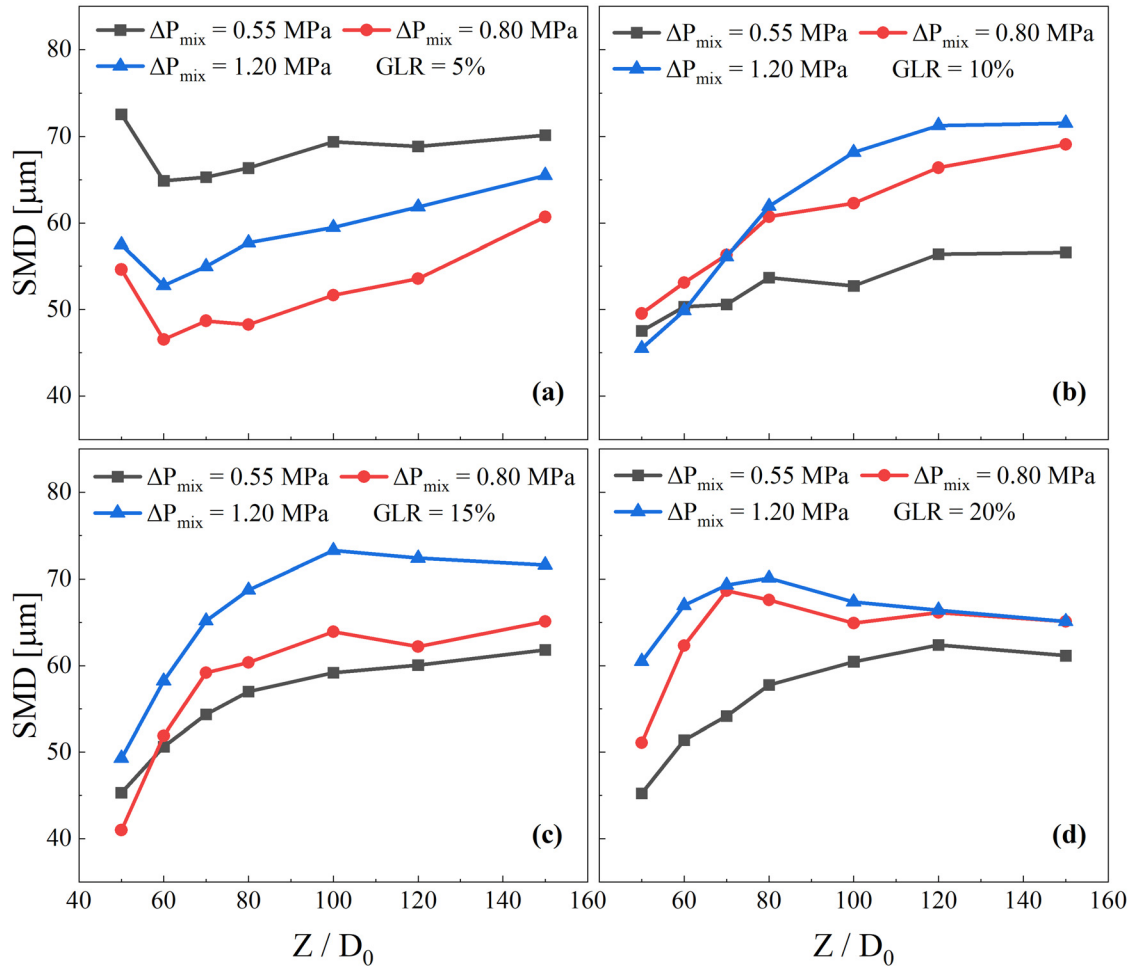


FIG. 23. Droplet SMD variations as a function of ΔP_{mix} at typical locations along the injector centerline for (a) GLR = 5%, (b) GLR = 10%, (c) GLR = 15%, and (d) GLR = 20%.

$$A^* = \frac{q_g \sqrt{T_0}}{K P_{inj}}, \tag{7}$$

where T_0 is the total temperature of the gas stream, K is 0.0397 for nitrogen gas, and P_{inj} is the absolute injection pressure. The equivalent diameter of the gas core d_g can be obtained by

$$d_g = \sqrt{\frac{4A^*}{\pi}}. \tag{8}$$

Since the diameter of the injector orifice d_0 is given, the equivalent average liquid film thickness at the throat can be obtained. When the gas is ejected from the injector orifice, the diameter of the gas core at the throat is the smallest, and the liquid film thickness is the largest correspondingly. The liquid film thickness at the throat is taken as the initial liquid film breaking thickness Δ_L when the liquid is issued from the injector,

$$\Delta_L = \frac{1}{2} (d_0 - d_g). \tag{9}$$

Considering the influence of initial liquid film thickness on SMD, a dimensionless parameter Δ_L/SMD is defined to measure the atomization efficiency, which quantifies the overall capability of the injector in scattering the initial liquid sheet into dispersed droplets under certain operating condition.

The Atomization efficiency Δ_L/SMD for two typical GLRs under various injection pressures is shown in Fig. 25. It can be observed that with increasing injection pressure, the injector scatters the initial liquid sheet into increasingly smaller droplets; however, the resultant SMD is more sensitive to the initial liquid sheet thickness Δ_L . The gas and liquid streams have to share the cross-sectional area of the injector orifice in the annular flow state; therefore, increasing the injection pressure will shrink the cross-sectional area occupied by the gas core flow and yield a thicker initial liquid sheet. This is the main reason for the increase in SMD with increasing injection pressure under the same GLR; this indicates that the SMD is mainly determined by Δ_L , whereas the atomization efficiency Δ_L/SMD is enhanced with increasing injection pressure.

According to the atomization mechanism and spray instability study in the present work, the main influential factors in the spray

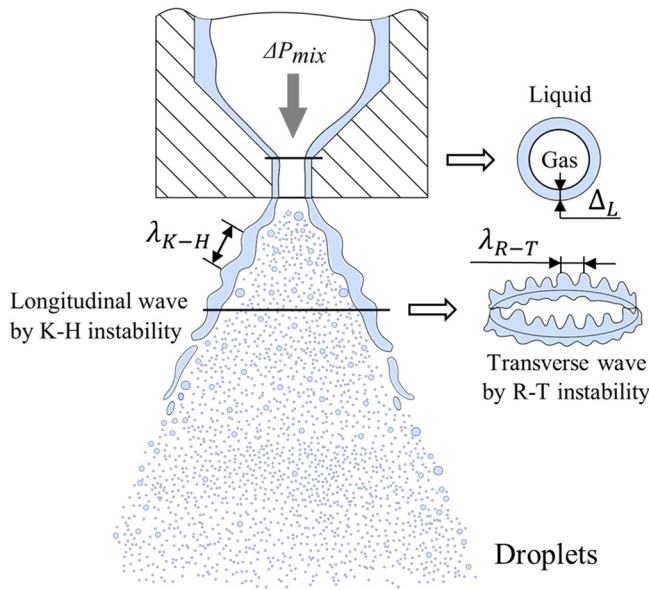


FIG. 24. Schematic to illustrate a possible mechanism for twin-fluid atomization in the annular flow regime.

characteristics of twin-fluid atomization can be deduced. Considering the geometric design of the twin-fluid injectors, the basic goal is to generate a thin liquid film inside the injector orifice. As such, increasing the length of the mixing chamber can effectively reduce the liquid film thickness in the mixing chamber; increasing the number of liquid injection holes can reduce the momentum ratio of liquid to gas per liquid injection hole⁵⁷ and improve the spray's stability. Moreover, reducing the ratio of injector orifice and mixing chamber diameter are advantageous for atomization, which yields smaller droplets.²⁷ Regarding the operating of the injectors in pragmatic conditions, the fuel rheological behavior may increase the wavelength of the K-H and R-T instability waves responsible for the atomization, which results in enlarged droplet sizes.⁵⁸ As for the thermos-physical properties,

according to the previous studies,⁵⁹ viscosity and surface tension would prevent ligaments from breaking up. Based on the atomization mechanism proposed in this work, increase in surface tension and viscosity will inevitably inhibit the growth of the K-H and R-T instability waves, which hinders the bulk liquid destabilization and subsequently ligament breakup.⁶⁰ This is consistent with previous studies by Ejim *et al.*⁶¹ for air-assisted atomization, whereas quantitative analyses on the influence of thermos-physical properties of the liquids on the twin-fluid atomization merit further systematic investigation.

IV. CONCLUDING REMARKS

In this study, the atomization characteristics of a twin-fluid injector operating in the annular flow regime were experimentally investigated under various GLRs and injection pressures. The macroscopic structure of the spray was visualized using a high-speed camera, while the droplet diameter and velocity were measured using PDPA. In addition, the flow state inside the injector was examined to reveal the underlying mechanism for the instability of the external spray. The major findings are summarized as follows.

The SCA of the twin-fluid injector increases almost linearly with GLR. Simultaneously, the droplet size first decreases and then increases along the axial direction; this is mainly due to the competition between droplet breakup, coalescence, and gaseous flow entrainment. Moreover, under the same injection pressure, the axial distance required for droplet coalescence to outweigh the breakup decreases with increasing GLR. Furthermore, estimation of the single-droplet shear Weber number indicates that shear breakup is less likely in the spray far field, and the droplet disintegration is predominately controlled by turbulent breakup under large Reynolds numbers in the range 10^4-10^5 .

The droplet sizes at different measurement positions tend to follow a lognormal distribution function. For a low GLR (3%), the droplet velocities follow a normal distribution function, whereas under large GLRs, the droplet velocity distribution is closer to a lognormal distribution function. Regarding the radial distribution, low GLRs (3% and 5%) lead to a bimodal spatial velocity distribution due to small SCAs, while for large GLRs, the droplet velocity decreases monotonically toward the far field.

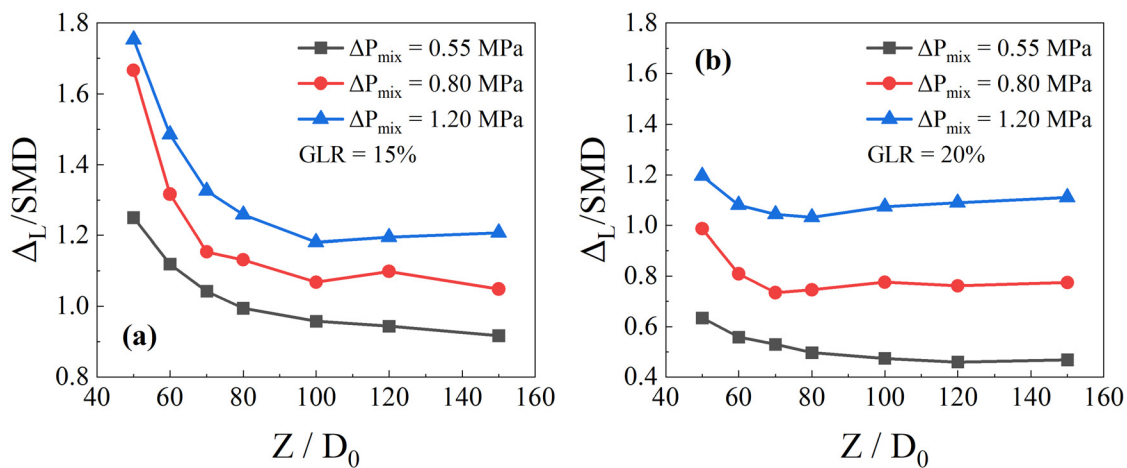


FIG. 25. Atomization efficiency Δ_L/SMD variations as a function of ΔP_{mix} at typical locations along the injector centerline for (a) GLR = 15% and (b) GLR = 20%.

Downloaded from http://pubs.aip.org/journal/phf/article-pdf/doi/10.1063/5.0128231/16602504/123309_1_online.pdf

The stability of the spray improves with increasing GLR. Furthermore, a higher injection pressure corresponds to a larger SCA and leads to a more stable spray; nevertheless, the droplet SMD increases under raised injection pressure. The atomization mechanism for a twin-fluid injector in the annular flow regime is equivalent to a successive process of K–H and R–T instabilities disintegrating the initial annular liquid sheet, which implies a direct proportionality between the SMD and initial liquid sheet thickness Δ_L . Correspondingly, for higher injection pressures, the central gas core shrinks and Δ_L increases; thus, the SMD enlarges, while the atomization efficiency Δ_L/SMD increases.

SUPPLEMENTARY MATERIAL

See the [supplementary material](#) for the following. (i) A detailed summary of the experimental conditions under various GLRs and ΔP_{mix} values. (ii) Statistical analysis of the droplet dynamics for GLR = 8% under $\Delta P_{\text{mix}} = 0.8$ MPa at the selected sampling locations, including scatter distributions of droplet diameters and velocities, and PDFs of droplet diameter and velocity. The selected locations mentioned above include Z/D_0 values of 50, 60, 75, and 100. (iii) Temporal evolutions of droplet velocities and arrival times for $Z/D_0 = 50$ under various ΔP_{mix} values and four typical GLRs, including $\Delta P_{\text{mix}} = 0.55$ and 1.20 MPa. The typical GLRs mentioned above include 3%, 8%, 15%, and 20%.

ACKNOWLEDGMENTS

The authors would like to acknowledge the research grant received from the National Natural Science Foundation of China (Grant No. 51806013), the Foundation Research Funds of the Ministry of Industry and Information Technology (Grant Nos. JCKY2019602D018 and WDZC-2019-JGKK-02), and the Beijing Institute of Technology Research Fund Program for Young Scholars (Grant No. 2020CX04047).

AUTHOR DECLARATIONS

Conflict of Interest

The authors have no conflicts to disclose.

Author Contributions

Chang Liu: Formal analysis (equal); Investigation (equal); Writing – original draft (equal). **Kun Wu:** Conceptualization (lead); Funding acquisition (equal); Methodology (equal); Supervision (equal); Writing – review & editing (equal). **Zhenyu Zhang:** Methodology (equal); Resources (equal). **Yueming Yuan:** Methodology (equal). **Xuejun Fan:** Funding acquisition (equal); Project administration (equal).

DATA AVAILABILITY

The data that support the findings of this study are available from the corresponding author upon reasonable request.

REFERENCES

1. J. Lee, K. C. Lin, and D. Eklund, “Challenges in fuel injection for high-speed propulsion systems,” *AIAA J.* **53**, 1405 (2015).
2. S. R. Turns, *An Introduction to Combustion: Concepts and Applications* (McGraw Hill Press, 1996).
3. K. C. Lin, M. C. Lai, T. Ombrello, and C. D. Carter, “Structures and temporal evolution of liquid jets in supersonic crossflow,” AIAA Paper No. 2017-1958, 2017.
4. Z. T. Zhao, W. Huang, L. Yan, and Y. G. Yang, “An overview of research on wide-speed range waverider configuration,” *Prog. Aerosp. Sci.* **113**, 100606 (2020).
5. C. J. Tam, S. C. Stouffer, K. C. Lin, M. Gruber, and T. Jackson, “Gaseous and liquid injection into high-speed crossflows,” AIAA Paper No. 2005-301, 2005.
6. C. Ghenai, H. Sapmaz, and C. X. Lin, “Characterization of aerated liquid jet in subsonic and supersonic cross flow,” AIAA Paper No. 2005-3580, 2005.
7. K. Miller, J. Sisco, N. Nugent, and W. Anderson, “Combustion instability with a single-element swirl injector,” *J. Propul. Power* **23**, 1102 (2007).
8. S. O. Macheret, M. N. Shneider, and R. B. Miles, “Plasma-Assisted fuel atomization and multipoint ignition for scramjet engines,” *J. Propul. Power* **36**, 357 (2020).
9. H. Wu, F. Zhang, and Z. Zhang, “Fundamental spray characteristics of air-assisted injection system using aviation kerosene,” *Fuel* **286**, 119420 (2021).
10. S. G. Daviault, O. B. Ramadan, E. A. Matida, P. M. Hughes, and R. Hughes, “Atomization performance of petroleum coke and coal water slurries from a twin fluid atomizer,” *Fuel* **98**, 183 (2012).
11. P. Stähle, V. Gaukel, H. P. Schuchmann, “Investigation on the applicability of the effervescent atomizer in spray drying of foods: influence of liquid viscosity on nozzle internal two-phase flow and spray characteristics,” *J. Food Process Eng.* **38**, 474 (2015).
12. K. C. Lin, K. Kirkendall, P. Kennedy, and T. Jackson, “Spray structures of aerated liquid fuel jets in supersonic crossflows,” AIAA Paper No. 1999-2374, 1999.
13. K. C. Lin and P. Kennedy, “Spray penetration heights of angle-injected aerated-liquid jets in supersonic crossflows,” AIAA Paper No. 2000-194, 2000.
14. G. Yu, J. G. Li, X. Y. Zhang, and C. J. Sung, “Investigation of liquid hydrocarbon combustion in supersonic flows using effervescent atomization,” AIAA Paper No. 2002 + 4279, 2002.
15. M. Chakraborty, A. Vaidyanathan, and S. L. N. Desikan, “Experiments on atomization and spray characteristics of an effervescent strut injector,” *Phys. Fluids* **33**, 017103 (2021).
16. S. D. Sovania, P. E. Sojka, and A. H. Lefebvre, “Effervescent atomization,” *Prog. Energy Combust.* **27**, 483 (2001).
17. A. H. Lefebvre, X. F. Wang, and C. A. Martin, “Spray characteristics of aerated-liquid pressure atomizers,” *J. Propul. Power* **4**, 293 (1988).
18. C. Sun, Z. Ning, X. Qiao, M. Lv, J. Fu, J. Zhao, and X. Wang, “Numerical simulation of gas–liquid flow behavior in the nozzle exit region of an effervescent atomizer,” *Int. J. Spray Combust.* **2019**, 11.
19. M. Zaremba, J. Kozák, M. Malý, L. Weiß, P. Rudolf, J. Jedelský, and M. Jicha, “An experimental analysis of the spraying processes in improved design of effervescent atomizer,” *Int. J. Multiphase Flow* **103**, 1 (2018).
20. C. Catlin and J. Swithenbank, “Physical processes influencing effervescent atomizer performance in the slug and annular flow regimes,” *Atomization Sprays* **11**, 575 (2001).
21. S. Menon and M. Gurnadhan, “Droplet behavior in overexpanded supersonic two-phase jets,” *Int. J. Multiphase Flow* **152**, 104076 (2022).
22. D. M. Wilson and W. Strasser, “A spray of puree: Wave-augmented transonic airblast non-Newtonian atomization,” *Phys. Fluids* **34**, 073108 (2022).
23. Z. W. Wu, Z. H. Shi, H. Zhao, F. Yao, H. F. Liu, W. F. Li, and J. L. Xu, “Effects of bubbles in the liquid jet on the air-blast atomization,” *Fuel* **266**, 117117 (2020).
24. P. Stähle, H. P. Schuchmann, and V. Gaukel, “Performance and efficiency of pressure-swirl and twin-fluid nozzles spraying food liquids with varying viscosity,” *J. Food Process Eng.* **40**, e12317 (2017).
25. A. Kleinhans, K. Georgieva, M. Wagner, V. Gaukel, and H. P. Schuchmann, “On the characterization of spray unsteadiness and its influence on oil drop breakup during effervescent atomization,” *Chem. Eng. Process.* **104**, 212 (2016).
26. M. Milkvik, P. Stähle, H. P. Schuchmann, V. Gaukel, J. Jedelsky, and M. Jicha, “Twin-fluid atomization of viscous liquids: The effect of atomizer construction on breakup process, spray stability and droplet size,” *Int. J. Multiphase Flow* **77**, 19 (2015).

- ²⁷F. A. Hammad, K. Sun, Z. Che, J. Jedelsky, and T. Wang, "Internal two-phase flow and spray characteristics of outside-in-liquid twin-fluid atomizers," *Appl. Therm. Eng.* **187**, 116555 (2021).
- ²⁸P. Dančová, M. Zaremba, M. Mlkvik, M. Malý, J. Jedelský, M. Jícha, and T. Vít, "Evaluation of steadiness and drop size distribution in sprays generated by different twin-fluid atomizers," *EPJ Web Conf.* **92**, 02118 (2015).
- ²⁹S. Chatterjee, M. Das, A. Mukhopadhyay, and S. Sen, "Experimental Investigation of Breakup of Annular Liquid Sheet in a Hybrid Atomizer," *J. Propul. Power* **31**, 1232 (2015).
- ³⁰H. Zhao, J. L. Xu, J. H. Wu, W. F. Li, and H. F. Liu, "Breakup morphology of annular liquid sheet with an inner round air stream," *Chem. Eng. Sci.* **137**, 412 (2015).
- ³¹S. Wachter, T. Jakobs, and T. Kolb, "Comparison of central jet and annular sheet atomizers at identical gas momentum flows," *Ind. Eng. Chem. Res.* **60**, 11502 (2021).
- ³²M. Wittner, H. Karbstein, and V. Gaukel, "Air-core-liquid-ring (ACLR) atomization: Influences of gas pressure and atomizer scale up on atomization efficiency," *Processes* **7**, 139 (2019).
- ³³J. S. Chin and A. H. Lefebvre, "A design procedure for effervescent atomizers," *J. Eng. Gas Turbines Power* **117**, 266 (1995).
- ³⁴L. Qian, J. Lin, and H. Xiong, "A fitting formula for predicting droplet mean diameter for various liquid in effervescent atomization spray," *J. Therm. Spray Technol.* **19**, 586 (2010).
- ³⁵H. Wu, F. Zhang, and Z. Zhang, "Droplet breakup and coalescence of an internal-mixing twin-fluid spray," *Phys. Fluids* **33**, 013317 (2021).
- ³⁶C. Tang, P. Zhang, and C. K. Law, "Bouncing, coalescence, and separation in head-on collision of unequal-size droplets," *Phys. Fluids* **24**, 022101 (2012).
- ³⁷A. Saha, J. D. Lee, S. Basu, and R. Kumar, "Breakup and coalescence characteristics of a hollow cone swirling spray," *Phys. Fluids* **24**, 124103 (2012).
- ³⁸J. H. Im, S. Cho, Y. Yoon, and I. Moon, "Comparative study of spray characteristics of gas-centered and liquid-centered swirl coaxial injectors," *J. Propul. Power* **26**, 1196 (2010).
- ³⁹J. C. Lasheras, E. Villermaux, and E. J. Hopfinger, "Break-up and atomization of a round water jet by a high-speed annular air jet," *J. Fluid Mech.* **357**, 351 (1998).
- ⁴⁰A. R. Hanson, E. G. Domich, and H. S. Adams, "Shock tube investigation of the breakup of drops by air blasts," *Phys. Fluids* **6**, 1070 (1963).
- ⁴¹L. P. Hsiang and G. M. Faeth, "Drop deformation and breakup due to shock wave and steady disturbances," *Int. J. Multiphase Flow* **21**, 545 (1995).
- ⁴²V. Ferrand, R. Bazile, J. Borée, and G. Charnay, "Gas-droplet turbulent velocity correlations and two-phase interaction in an axisymmetric jet laden with partly responsive droplets," *Int. J. Multiphase Flow* **29**, 195 (2003).
- ⁴³J. O. Hinze, "Fundamentals of the hydrodynamic mechanism of splitting in dispersion processes," *AIChE J.* **1**, 289 (1955).
- ⁴⁴S. K. Sahoo and H. Gadgil, "Hydrodynamic response of an annular swirling liquid sheet surrounding a forced gas jet," *J. Fluid Mech.* **947**, A20 (2022).
- ⁴⁵J. P. Matas, A. Delon, and A. Cartellier, "Shear instability of an axisymmetric air-water coaxial jet," *J. Fluid Mech.* **843**, 575 (2018).
- ⁴⁶S. Wachter, T. Jakobs, and T. Kolb, "Towards system pressure scaling of gas assisted coaxial burner nozzles—An empirical model," *Appl. Energy Combust. Sci.* **5**, 100019 (2021).
- ⁴⁷J. Jedelsky and M. Jícha, "Energy conversion during effervescent atomization," *Fuel* **111**, 836 (2013).
- ⁴⁸A. A. Rizkalla and A. H. Lefebvre, "The influence of air and liquid properties on airblast atomization," *J. Fluids Eng.* **97**, 316 (1975).
- ⁴⁹P. Marmottant and E. Villermaux, "On spray formation," *J. Fluid Mech.* **498**, 73 (2004).
- ⁵⁰A. Kumar and S. Sahu, "Large scale instabilities in coaxial air-water jets with annular air swirl," *Phys. Fluids* **31**, 124103 (2019).
- ⁵¹Y. Li, M. Zhang, and K. Wu, "Three-dimensional simulation of ligament formation and breakup caused by external vibration," *Phys. Fluids* **32**, 083605 (2020).
- ⁵²S. Arnaud, J. P. Matas, and A. Cartellier, "Study of axial and transverse instabilities in assisted atomization," in *6th International Conference on Multiphase Flow (ICMF)*, 2007.
- ⁵³L. J. Yang, Y. P. Gao, J. X. Li, and Q. F. Fu, "Theoretical atomization model of a coaxial gas-liquid jet," *Phys. Fluids* **32**, 124108 (2020).
- ⁵⁴N. K. Rizk and A. H. Lefebvre, "The influence of liquid film thickness on airblast atomization," *J. Eng. Gas Turbines Power* **102**, 706 (1980).
- ⁵⁵J. Anderson, *Fundamentals of Aerodynamics* (McGraw Hill Press, 2010).
- ⁵⁶S. J. Peltier, K. C. Lin, C. D. Carter, and A. L. Kastengren, "Characterization of the external and internal flow structure of an aerated-liquid injector using x-ray radiography and fluorescence," *Exp. Fluids* **58**, 111 (2017).
- ⁵⁷S. H. Song and S. Y. Lee, "Study of atomization mechanism of gas liquid mixtures," *Atomization Sprays* **6**, 193 (1996).
- ⁵⁸S. C. Geckler and P. E. Sojka, "Effervescent atomization of viscoelastic liquids: experiment and modeling," *J. Fluids Eng.* **130**, 061303 (2008).
- ⁵⁹D. Konstantinov, R. Marsh, P. Bowen, and A. Crayford, "Effervescent atomization for industrial energy-technology review," *Atomization Sprays* **20**, 525 (2010).
- ⁶⁰F. Liu, N. Kang, and Y. Li, "Numerical investigation on the mechanism of ligament formation aroused by Rayleigh-Taylor instability," *Comput. Fluids* **154**, 236 (2017).
- ⁶¹C. E. Ejim, M. A. Rahman, A. Amirfazli, and B. A. Fleck, "Effects of liquid viscosity and surface tension on atomization in two-phase, gas/liquid fluid coker nozzles," *Fuel* **89**, 1872 (2010).